DOI: 10.1002/ ((please add manuscript number))
Article type: Full Paper

Disentangling Epitaxial Growth Mechanisms of Solution Derived Functional Oxide Thin Films

Albert Queraltó, Maria de la Mata, Jordi Arbiol, Xavier Obradors, Teresa Puig*

Dr. A. Queraltó, Dr. M. de la Mata, Prof. Dr. X. Obradors, Prof. Dr. T. Puig
Institut de Ciència de Materials de Barcelona, Consejo Superior de Investigaciones Científicas (ICMAB-CSIC), Campus UAB, 08193 Bellaterra, Catalonia, Spain.
E-mail: albert.queralto.lopez@gmail.com

Dr. M. de la Mata, Prof. Dr. J. Arbiol
Catalan Institute of Nanoscience and Nanotechnology (ICN2), CSIC and The Barcelona Institute of Science and Technology (BIST), Campus UAB, Bellaterra, 08193 Barcelona, Catalonia, Spain

Prof. Dr. J. Arbiol
Institució Catalana de Recerca i Estudis Avançats (ICREA), Passeig Lluís Companys 23, 08010 Barcelona, Catalonia, Spain

Keywords: chemical solution deposition, epitaxial crystallization, functional oxides, rapid thermal annealing

ABSTRACT

We have investigated the mechanisms of epitaxial development and functional properties of oxide thin films ($Ce_{0.9}Zr_{0.1}O_{2-y}$, $LaNiO_3$ and $Ba_{0.8}Sr_{0.2}TiO_3$) grown on single crystal substrates (Y_2O_3:ZrO_2, $LaAlO_3$ and $SrTiO_3$) by the chemical solution deposition approach. Rapid thermal annealing furnaces are very powerful tools in this study providing valuable information of the early stages of nucleation, the kinetics of epitaxial film growth and the coarsening of nanocrystalline phases. Advanced transmission electron microscopies, x-ray diffraction and atomic force microscopy are employed to investigate the film microstructure and morphology, microstrain relaxation and epitaxial crystallization. We demonstrate that the isothermal evolution towards epitaxial film growth follows a self-limited process driven by atomic diffusion, and surface and interface energy minimization. All investigated oxides

experience a transformation from the polycrystalline to the epitaxial phase. We unequivocally evidence that the film thickness highly influences the epitaxial crystallization rate due to the competition between heterogeneous and homogeneous nucleation barriers and the fast coarsening of polycrystalline grains as compared to epitaxial growth. The investigated films possess good functional properties, and we successfully confirmed an improvement at long annealing times that can be correlated with grain boundary healing processes. Thick epitaxial films can be crystallized by growing sequential individual epitaxial layers.

1. Introduction

Epitaxial complex functional oxides (e.g. $La_{1-x}Sr_xMnO_3$, $Ba_{1-x}Sr_xTiO_3$, $PbZr_xTi_{1-x}O_3$, $BiFeO_3$, $YBa_2Cu_3O_{7-x}$, CeO_2, $LaNiO_3$, etc) are valuable candidates for the fabrication of novel devices in multiple applications due to the broad variety of chemical and physical properties exhibited such as ferromagnetism, ferroelectricity, colossal magnetoresistance, multiferroicity, superconductivity, buffer layers in heterostructures or coated conductors, ionic conductivity, resistive RAM memories and catalysis.[1] Physical techniques like sputtering or pulsed laser deposition are often used to grow epitaxial oxide materials and heterostructures, but they require expensive vacuum systems. Chemical solution deposition (CSD) is an appealing methodology for the fabrication of oxide devices that provides significant advantages being a versatile and low-cost alternative that allows deposition over large areas and provides good stoichiometric control.[2] For instance, inkjet printing is an innovative approach combining the advantages of solutions based methods with the fast, industrial-oriented production of electronic and functional oxide devices on organic and inorganic flexible substrates (e.g. plastic, metals, paper or textile).[3]

The scientific and industrial relevance of CSD for functional oxide growth has driven researchers to study the fundamental thermodynamic and kinetic aspects associated to it. Particularly, there have been notable contributions to study the mechanisms leading to the

self-assembling of epitaxial oxide nanoislands,[2c, 2d, 4] establishing a solid background for more complex film growth. Some works have studied the crystallization kinetics of polycrystalline oxide films such as lead zirconium titanate (PZT) and cerium oxide.[5] Also, even if an enormous effort has been dedicated to understand the epitaxial growth of high-temperature superconducting yttrium barium copper oxide (YBCO) films,[2e, 6] there still exists few knowledge on the epitaxial development of solution derived functional oxides. Conventional sample processing in CSD is based on electrical resistance furnaces, also known as conventional thermal annealing or CTA. These furnaces have a large thermal inertia which leads to long temperature stabilization times and slow heating/cooling ramps around 0.05-0.5 ºC s^{-1} (3-30 ºC min^{-1}). Thus, a strong microstructural evolution cannot be avoided during heating cycles. Instead, rapid thermal annealing (RTA) furnaces, where sample heating is done through infrared lamp furnaces, develop heating/cooling ramps orders of magnitude faster (1-250 ºC s^{-1}), therefore, offering many advantages to investigate the mechanisms of epitaxial film crystallization and to achieve unique processing paths. For instance, RTA has proven useful to lower the crystallization temperature and time of PZT films by preventing the formation of an intermediate phase slowing down the perovskite phase formation or in the fabrication of thick oxide films for electronic devices.[5a, 7] Although RTA seems ideal for the study of epitaxial oxide crystallization, most of the reported works have been related up to now to oxide polycrystalline film growth, for instance ZrO_2, $PbZr_xTi_{1-x}O_3$ or $SrBi_2Ta_2O_9$.[8] Heteroepitaxial growth involves single crystal substrates and high temperature thermal treatments and it is desired over polycrystalline growth in many film functionalities where physical properties are highly influenced by structural and chemical disorder associated to grain boundaries.[9] A precise control of the crystalline quality, induced strain and film microstructure which are highly dependent on the processing conditions is also needed in order to fabricate functional devices with excellent performances. This work reports on a new insight on the thermodynamic and kinetic mechanisms governing the epitaxial crystallization

of functional oxides derived from chemical solutions by using RTA to precisely control their microstructural evolution from the amorphous/nanocrystalline phases obtained after the decomposition of the solution precursors. In order to provide a general perspective of the phenomena involved, we investigate multiple epitaxial oxide systems displaying different functionalities and nucleation modes. Zirconium-doped ceria ($Ce_{0.9}Zr_{0.1}O_{2-y}$ or CZO) grown on yttria-stabilized zirconia (Y_2O_3:ZrO_2 or YSZ), lanthanum nickelate ($LaNiO_3$ or LNO) on strontium titanate ($SrTiO_3$ or STO), and barium strontium titanate ($Ba_{0.8}Sr_{0.2}TiO_3$ or BST) on lanthanum aluminate ($LaAlO_3$ or LAO). These systems are chosen because of their chemical and structural compatibility, due to the relatively small lattice mismatches favorable for epitaxial growth, i.e. -4.5% for CZO/YSZ, 1.4% for LNO/STO and -5.1% for BST/LAO, and their remarkable functional properties. Ceria-based oxide films are often used in electronic devices or in high temperature superconducting coated conductors due to their high dielectric constant, mechanical and chemical stability.[6b, 6c, 10] The application of CZO in oxygen sensors, solid-oxide fuel cells, solar thermochemical hydrogen generation, oxygen buffer and active support for noble metals in catalysis is also under investigation.[1e, 11] Lanthanum nickelate ($LaNiO_3$ or LNO) is used for the integration of oxide materials with silicon and as electrode in electronic devices due to its low electrical resistivity at room temperature.[12] Barium strontium titanate ($Ba_{0.8}Sr_{0.2}TiO_3$ or BST) possesses highly remarkable optical and dielectric properties and it is being used in non-linear optics, infrared detectors, thermal imaging, microwave dielectrics or capacitors.[13] BST also shows ferroelectric response at room temperature for Ba/Sr ratios above 0.7/0.3.[13a, 14]

We have conducted systematic investigations to evaluate the film morphology and microstructural relaxation at different experimental conditions, i.e. annealing times and film thickness. Two-dimensional X-ray diffraction (2D-XRD) measurements are performed to evaluated and quantify the transformation to the epitaxial structure and correlate it with the microstructure. The results are supported by appropriate thermodynamic and kinetic

theoretical descriptions. Finally, we have measured the functional properties of the films and correlated the results with those from the film microstructure and epitaxial growth.

2. Results and discussion

2.1. Grain growth and microstructural relaxation

Thermal treatments by conventional or rapid thermal annealing have heat radiation as the source for film growth. We performed, first of all, crystallization experiments with both types of furnaces using the same heating rates. We verified that, indeed, no significant differences exist for films processed at the same conditions. This is demonstrated in **Figure S1** (Supplementary Material) which shows equivalent film morphologies, root mean square (RMS) roughness and XRD peak intensities for BST films grown on LAO substrates. CTA and RTA furnace treatments are done at 900 ºC, 0.5 ºC s^{-1} for 30 min in oxygen ambient. Equivalent experiments for CZO and LNO films have reported similar results.[15] Thus, tubular furnaces will be employed only where long annealing times are required.

In order to investigate epitaxial film development, we have performed isothermal annealing experiments with different durations, after annealing at very fast heating ramps with RTA (20 ºC s^{-1}). This heating ramp has been used recently to analyze separately nucleation and coarsening phenomena of oxide nanostructures,[2c, 15] and it was found that RTA is fast enough to avoid any significant coarsening during the heating ramp (~35-45 s in the present case). Therefore, it is very likely that a similar phenomenology holds for films.

The AFM characterization of BST films grown on LAO substrates by RTA (900 ºC, 20 ºC s^{-1} in O_2 for 1, 5 and 30 min) shows the morphological evolution of films with time and film thickness (**Figure 1a**). We observe a transformation with time from rounded grains to flat terraces and a denser structure reflecting an improved coalescence of the 3D nucleated grains after epitaxial growth.[1c, 2a] AFM images of CZO and LNO films grown on YSZ and STO

substrates at 900 and 700 ºC, respectively, show an equivalent morphological transformation of the film surface (**Figure S2**). CZO film growth is also 3D, while we will see later that 2D nucleation may occur in LNO films. Data analysis reveals that the grain dimensions (Figure 1b) increase approximately from 13 to 60 nm (CZO), 16 to 50 nm (LNO), and 24 to 90 nm (BST). On the other hand, Figure 1c shows a decrease of films RMS roughness with the annealing time from around 1.4 to 0.7 nm (CZO), 1.5 to 0.7 nm (LNO), and 6.5 to 3.0 nm (BST). Generally, grain coarsening is associated with an increase of the RMS roughness due to the presence of spherical grains and a progressively larger peak-to-valley difference.[16] However, kinetic mechanisms present during grain growth such as atomic mobility and grain boundary (GB) zipping processes help lowering the RMS roughness in epitaxial growth.[17] In this case, surface energy minimization is the driving force leading to the formation of flat terraces, thus, influencing roughness reduction.[2c, 5c, 6b, 18] The presence of some large grains is likely causing the unusually high film roughness for the BST case.

The growth rate of grains slightly decreases over time anticipating that a maximum grain size should be achieved. Since grain growth is a kinetic process associated to the movement of GBs,[19] crystalline defects and the dependence of atomic diffusion with grain size are frequently factors that limit GB migration, especially in the nanometer range. Previous works have referred to this behavior as self-limited growth which is described by a phenomenological law of the kinetic evolution of grain sizes:[5c, 5e, 5f, 20]

$$S(t) - S_0 = (S_{\max} - S_0)\left[1 - \exp\left(\frac{-t}{\tau_S}\right)\right] \qquad (1)$$

where S_0 and S_{max} are respectively the initial and final grain diameter, t is the instantaneous time, and τ_S is the characteristic relaxation time at $S(t)=0.63S_{max}$. The specific τ_S values are: 2000 (CZO), 1680 (LNO) and 1630 s (BST). The atomic diffusion coefficients D can also be calculated applying the equation

$$D = \frac{\left(S_{\max} - S_0\right)^2}{4\tau_S}. \qquad (2)$$

The calculated diffusion coefficients for CZO, LNO and BST are respectively $(3.3\pm0.6)\times10^{-19}$, $(1.6\pm0.9)\times10^{-19}$ and $(9.4\pm0.7)\times10^{-19}$ m^2 s^{-1} at their annealing temperatures (900 ºC for CZO and BST, and 700 ºC for LNO). These numbers reveal that atoms diffuse significantly faster in BST films than in CZO films. It is also important to highlight that diffusion in LNO films is high; despite they are produced at temperatures 200 ºC lower than CZO and BST. Overall, these diffusion coefficients are approximately one order of magnitude larger than those reported for polycrystalline CeO_2 and $Ce_{1-x}Gd_xO_2$ (CGO) films grown by CTA (900 ºC, 3 ºC min^{-1}).[5c] Some works have proposed that the heating ramp highly influences nucleation and crystallization rates leading to different kinetic evolutions in films processed by RTA.[5a, 21] We will show later that epitaxial growth could also be related with the origin of the fast kinetics.

Film thickness has also a great influence over the microstructural evolution, and thus, the surface morphology. It has been reported previously in polycrystalline films that grains enlarge with film thickness and, consequently, surfaces become rougher.[5f, 22] Thicker films are prepared using the procedure described in the Experimental section. After 3 depositions, thicknesses are expected to be 60 nm (CZO), 70 nm (LNO) and 100 nm (BST), i.e. thrice the thickness of single coatings (**Figure S3**). Figure 1a and Figure S2 illustrate the surface morphology of thicker CZO, LNO and BST three-layer films grown by RTA for 30 min. The flat terraces observed in single-layer coatings disappear and film surfaces present more rounded grains. Unexpectedly, grain dimensions also become smaller than in single-layer films, from 60 to 25 nm (CZO), 50 to 20 nm (LNO), and 90 to 75 nm (BST). We will see later that these quasi-spherical grains very likely correspond to polycrystalline phases which are usually smaller than epitaxially terraced grains. As a result, the RMS roughness (Figure 1c) rises significantly compared to equivalent single-layer coatings from 0.7 to 2.1 nm (CZO), 0.7

to 3.0 nm (LNO) and 3.0 to 4.9 nm (BST). This is caused by the larger peak-to-valley difference as mentioned before. Another parameter which is significantly correlated to the microstructural evolution of epitaxial films is the RMS microstrain, i.e. the standard deviation of atomic positions from the mean value.[23] The microstrain μ, i.e. strain associated to the local distortions of the lattice, is particularly influenced by grain coarsening and GB zipping processes.[23] The determination of RMS μ values is done for single-layer epitaxial films by evaluating the peak broadening of (*00l*) reflections in θ-2θ scans with the Williamson-Hall method (**Figure S4**).[23] **Figure 2a** shows that μ depends on the particular oxide and also that it decreases with the annealing time. The evolution can be described with an exponential decay function:[5c]

$$\mu = \mu_r + \mu_0 \exp\left(\frac{-t}{\tau_\mu}\right), \qquad (3)$$

where μ_r and μ_0 are the residual and initial microstrain, and τ_μ is the relaxation time. CZO has a larger μ_0 than LNO and BST, while μ_r values are almost identical (~0.2-0.3 %). This means that CZO films have an increased number of disordered GBs, as compared to LNO and BST films. τ_μ values for CZO, LNO and BST films are approximately 400, 370 and 60 s, respectively; much shorter than the relaxation times for grain coarsening. This suggests that grain coarsening continues after the residual microstrain has been stabilized. Essentially, microstrain evolution reflects healing of defects at GBs while grain coarsening involves GB displacement. The faster microstrain relaxation of BST, as compared to CZO and LNO, can be related to a larger atomic diffusion during the GB zipping process. Equivalent values of μ have been reported by Rupp *et al.* for CGO films grown by CTA (900 ºC, 3 ºC min^{-1}).[5c] However, the relaxation is significantly faster in our films grown by RTA. As we mentioned before, this could be related to the fast RTA heating ramps and the modification of nucleation and crystallization rates, as reported elsewhere.[5a, 21]

2.2. Transformation to epitaxial oxide films

Crystal growth in CSD films is thermodynamically driven by a decrease in the Gibbs free energy from the initial amorphous/nanocrystalline phase to the final crystalline film.[2b-d] The energy provided through thermal annealing allows overcoming the heterogeneous nucleation barrier responsible of the epitaxy development throughout the film thickness.[2b] In our case, the temperatures selected ensure that films achieve a complete epitaxial growth. The parameters involved in this crystallization process are atomic diffusion, interfacial, surface and elastic energies minimization and GB recrystallization.[24]

Figure 2b, **S5a** and S5c show the XRD diffraction patterns for single layers of CZO on (001) YSZ, LNO on (001) STO and BST on (001) LAO heterostructures at different annealing times. We observe the (002) reflection of YSZ, STO and LAO substrates at 35.0º, 46.5º and 48.0º, and the weak signal associated to the K_β reflection at 31.4º, 41.8º and 43.1º. The (002) reflections of CZO (33.4º), LNO (47.3º) and BST (45.9º) are also present. The (002) film peak intensities grow with the annealing time; a phenomenon more pronounced at short annealing times, also revealing very high crystallization speeds. In addition, we can identify a very weak (111) CZO orientation at 28.8º for annealing times below 10 min which disappears for longer treatments. No other orientations are observed for LNO and BST besides (002) peaks. Three-layer films present comparable (002) intensities as illustrated in Figure 2c, S5b and S5d, whereas the intensity of (111) CZO reflection is stronger. We also detect other peaks associated to (011) LNO, (011) and (111) BST orientations. The shift observed in the (002) LNO reflection (Figure S5c and S5d) is caused by film relaxation mechanisms discussed elsewhere.[15, 25] These results would suggest that films have grown epitaxially, as we will see later by TEM and 2D-XRD.

The growth mode of a film on top of a substrate can be predicted from a thermodynamic point of view by evaluating the wetting condition of a film on a substrate. The wetting condition is derived from Young's equation and it is defined as the change in surface energy $\Delta\gamma=\gamma_f+\gamma_i-\gamma_s$,

where γ_f, γ_i and γ_s are respectively the surface energies of the film, the film-substrate interface, and the substrate.[26] If we reach a full wetting condition ($\gamma_f+\gamma_i<\gamma_s$), the growth mode will be 2D or *layer-by-layer*, whereas if $\gamma_f+\gamma_i>\gamma_s$ the system will grow following a 3D or *Volmer-Weber* growth mode. We can consider that γ_f and γ_s correspond the energy of the (001) surface since it is the orientation of the single crystals employed, but also the epitaxial orientation of films. The interface energies for the heterostructures evaluated is considered close to 0 J m^{-2} since films are grown on substrates with the same crystallographic structure (fluorite/fluorite and perovskite/perovskite). CZO should present a 3D growth since γ_{CZO}=3.25 J m^{-2} and γ_{YSZ}=1.75 J m^{-2},[27] while the growth mode of LNO and BST films should be *layer-by-layer* (γ_{LNO}=1 J m^{-2}<γ_{STO}=1.2 J m^{-2} and γ_{BST}=1.13 J m^{-2}<γ_{LAO}=1.58 J m^{-2}) [28]. **Figure 3** illustrates the HRTEM analysis of the single-layer oxide films investigated. CZO films annealed at 900 ºC, 20 ºC s^{-1} for 10 min in O_2 have areas where the film is completely epitaxial (Figure 3a). Figure 3b shows another region presenting truncated CZO pyramids, common of 3D Volmer-Weber epitaxial growth,[2c] together with particles of around 5-10 nm further up from the substrate. The power spectrum in Figure 3c confirms the random orientation of the particles, as well as the epitaxial orientation of nanopyramids. These pyramids are fully relaxed on top of the YSZ substrate with a lattice parameter $a_{CZO,exp}$=$a_{CZO,bulk}$=5.385 Å ($a_{YSZ,bulk}$=5.143 Å). Similar studies have been conducted on LNO films grown at 700 ºC, 20 ºC s^{-1} for 10 min in O_2. Figures 3d-f show that most of the film is epitaxial with some polycrystalline regions of around 10 nm close to the surface. In addition, it seems that LNO grows following a 2D layer-by-layer growth mode, confirming the results obtained from the wetting condition. The layer-by-layer growth is better observed from the flat surfaces in **Figures 4a** and 4b which show the AFM image and corresponding line scan of a LNO film obtained from a diluted precursor solution with a concentration of 0.04 M and annealed at 700 ºC, 10 ºC min^{-1} for 1 h in O_2. The epitaxial region of the LNO film is strained to match the STO substrate with a lattice parameter $a_{LNO,exp}$=$a_{STO,bulk}$=3.903 Å ($a_{LNO,bulk}$=3.850 Å), as calculated from the power

spectrum in Figure 3e. The HRTEM characterization of a single-layer BST film, annealed at 900 ºC, 20 ºC s^{-1} for 5 min in O_2, reveals a completely epitaxial film (Figure 3g and h). The power spectrum in Figure 3h reveals a fully relaxed BST film ($a_{BST,exp}$=$a_{BST,bulk}$=3.993 Å) on top of the LAO substrate ($a_{LAO,bulk}$=3.790 Å). Interestingly, Figure 4c-e shows that BST films follow a 3D Volmer-Weber growth instead of the 2D layer-by-layer growth calculated from the wetting condition. It has been reported before that strain can have a relevant influence in nucleation barriers, film morphology and epitaxial growth.[2a, 2c, 29] The surface and interface energies considered before are usually for unstrained nuclei. It has been suggested that an additional energy term in γ_f should be included to account for the contribution of strain:[30]

$$\gamma_f^{str} = \gamma_f + \sum_{i,j} \sigma_{ij} \varepsilon_{ij} + \frac{1}{2} \sum_{ijkl} \varepsilon_{ij} S_{ijkl} \varepsilon_{kl} \quad (4)$$

where σ_{ij} is the surface stress tensor, ε_{ij} the lattice mismatch and S_{ijkl} is the second order stress tensor. But also, the influence of strain in γ_i must be considered:[29b]

$$\gamma_i^{str} = \gamma_i + E_{str} + E_{dis} \quad (4)$$

where E_{str} is the interface strain energy per unit area and E_{dis} is the misfit dislocation energy per unit area. If we consider the lattice mismatch between film and substrate ($\varepsilon \sim a_{substrate}$-$a_{film}/a_{film}$; a_{film} and $a_{substrate}$ are the lattice parameters of film and substrate, respectively), we can see that LNO films on STO have a relatively low mismatch ($\varepsilon_{LNO\text{-}STO}$~1.4%) which may lead to a small strain energy enough to prevent a 3D growth. On the other hand, the strain energies of CZO on YSZ and BST on LAO should be significantly large given that the lattice mismatch are $\varepsilon_{CZO\text{-}YSZ}$~ -4.5% and $\varepsilon_{BST\text{-}LAO}$~ -5.1%. Thus, it would be feasible that the nucleation of BST films on LAO transitions from a 2D to a 3D growth mode.

The results shown until now clearly demonstrate that RTA is an adequate tool to fabricate and study epitaxial crystallization which occurs at very short annealing times. Despite that, an accurate evaluation of the epitaxial growth requires the use of more general tools not limited

to out-of-plane information or local regions of films such as 1D-XRD and HRTEM. The degree of epitaxy can be precisely calculated with a methodology that uses a 2D-XRD detector.[31] 2θ-χ scans are conducted at fixed φ angles to simultaneously collect multiple film crystalline orientations. The amount of (001) film crystallites aligned with the (001) substrate orientation ($I_{epitaxial}$) in relation to polycrystalline orientations (I_{random}) is quantified employing the equations:[1d, 31]

$$\frac{I_{random}}{I_{epitaxial}} = \frac{I_{ring}^{\exp}\left(360/\Delta\chi\right)4\pi}{8I_{epi}^{\exp}} \quad (5)$$

$$I_{random} + I_{epitaxial} = 100\ (\%) \quad (6)$$

$I_{epi}^{\exp}$ and $I_{ring}^{\exp}$ are the diffracted intensities of the epitaxial and polycrystalline phases for the same Bragg reflection, and $\Delta\chi$ is the angular range acquired for the misoriented crystallites. **Figure 5a** shows the quantification of the epitaxial fraction for BST films with one and three layers. Two examples of the 2D-XRD data used for the calculations are illustrated in Figure 5b and 5c. The epitaxial components of films and substrates, and polycrystalline material are displayed as a central "spot" and a ring, respectively. Equivalent studies for CZO and LNO films can be found in the Supporting Information (**Figure S6**). We observe that the epitaxial fraction in one-layer films grows rapidly at expenses of the polycrystalline material. Full epitaxy is reached after 15-30 min of annealing by RTA for CZO and LNO films, whereas epitaxial growth is completed after ~5-10 min for BST films. Instead, films with three layers show a slower evolution towards full epitaxy (Figure 5a and S6). Interestingly, the amount of time required to achieve complete epitaxial growth for single-layers is shorter than the time needed to reach full microstrain relaxation which is approximately around 1-2 h for CZO and LNO, and 30 min for BST (Figure 2a). Equivalent results have also been reported for YBCO films grown by conventional thermal annealing of chemical solutions.[6a] Therefore, these

results indicate that healing of GB defects is still in progress after films are completely epitaxial. **Figure S7** shows 2D-XRD (022)-centered pole figure measurements for CZO, LNO and BST films respectively grown on YSZ, STO and LAO substrates at 20 ºC s^{-1}, and temperatures of 900 ºC (CZO and BST) and 700 ºC (LNO). The annealing times are 30 min for CZO and LNO, and 45 min for BST films. These results indicate that CZO, LNO and BST films have four poles at χ=45º corresponding to the (002) orientation characteristic of epitaxial growth. No other signal has been detected, thus, confirming the achievement of full epitaxy in our films. After a good optimization process, the final epitaxial films are very compact and have very low residual porosity as demonstrated previously.[2c, 5d, 32]

Homogeneous and heterogeneous nucleation events (polycrystalline and epitaxial crystallization) may have similar probabilities since processing temperatures are far from the oxide melting point ($T_{mp,CZO}$~2400 ºC, $T_{mp,LNO}$~1680 ºC, $T_{mp,BST}$~1625 ºC [33]).[2b, 2d] However, the results indicate that there is a strong driving force to transform highly energetic polycrystalline material into an ordered epitaxial film with reduced surface and interface energies. Up to our knowledge, this is the first time that epitaxial growth is suggested to derive from polycrystalline material of the very same oxide phase in the case of binary oxides. For at least some ternary oxides such as YBCO,[2e, 34] this process clearly involves several intermediate phases.

The self-limited growth model described previously [Equations (1) and (2)] is also used to describe the crystallization kinetics from data in Figure 5a and S6. Comparison of the epitaxial diffusion coefficients (D_{epi}) of one- and three-layer CZO, LNO and BST films (**Figure 6a**) show a faster crystallization kinetics of one-layer BST films compared to LNO and CZO, as it could be envisaged from HRTEM results in Figure 3. This trend is also maintained for three-layer films which show a reduction in D_{epi} of about one order of magnitude. We have also extracted the transformation rates by converting the epitaxial fraction percentage to epitaxial film thickness, i.e. multiplying by the film thickness reported

before. Figure 6b illustrates an equivalent behavior to that described for the epitaxial diffusion coefficients. The initial values of the epitaxial growth rates for one-layer films range from 0.04 nm s^{-1} (CZO) to 0.2 nm s^{-1} (BST), while three-layer films have epitaxial growth rates more than one order of magnitude smaller [from 0.001 nm s^{-1} (CZO) to 0.01 nm s^{-1} (BST)]. Interestingly, there is a decrease of the epitaxial growth rates with the annealing time. This could be understood as a reduction in the driving force towards epitaxy as the transformation proceeds due to microstructural evolution of the remaining polycrystalline material being available for recrystallization.

The interpretation of these results involves several factors. The simple evaluation of the ratio between growth temperature and melting point (T/T_{mp}) for each oxide confirms that the atomic mobility of BST ($T/T_{mp,BST}$~0.55) must be larger than that of LNO ($T/T_{mp,LNO}$~0.42) and CZO ($T/T_{mp,CZO}$~0.38). The measurement of the polycrystalline particle size for three-layer films could help explain the reduction with time of the epitaxial growth rates. It is worth mentioning that the transformation of a polycrystalline phase to epitaxial material involves a reorientation or recrystallization of grains. These processes are more difficult for large grains and, therefore, epitaxial growth should be slowed down. Figure 6c presents the Debye-Scherrer analysis performed on the polycrystalline peaks from Figure 2c and S5b and S5d, i.e. (111) CZO, (011) LNO and (011) BST reflections. We observe coarsening of the polycrystalline grains with the annealing time. Specifically, CZO films show a much larger growth, from 15 nm after 30 min of annealing to 32 nm after 240 min, while the polycrystalline grain dimensions of LNO and BST evolve with a much contained growth; from 12 and 16 nm after 30 min of annealing, and 16 and 22 nm after 240 min. Figure 6d shows the polycrystalline diffusion coefficients (D_{poly}) calculated from data fitting of Figure 6c with the self-limited growth model described previously. These are effective values of atomic diffusion since many parameters have an influence over it (grain boundaries, porosity, etc). $D_{poly,CZO}$ is almost two times larger than $D_{poly,LNO}$ and $D_{poly,BST}$ as expected from the grain

sizes in Figure 6c. These results confirm our suspicions; epitaxial crystallization of CZO is slower compared to LNO and BST due to a faster polycrystalline grain coarsening. Full epitaxial growth should be possible in three-layer films since D_{epi} are more than one order of magnitude larger than D_{poly}. Our data predicts that the epitaxial growth of CZO, LNO and BST films should be completed after long annealing times in the range of 80, 16 and 10 h, respectively. **Figure 7** illustrates the process towards epitaxial growth. Essentially, epitaxy proceeds as long as polycrystalline grains are small. Otherwise, it is slowed down and longer annealing times will be required to achieve complete epitaxial films. Nucleation barriers are also a factor to consider in epitaxial crystallization. The calculation of heterogeneous and homogeneous nucleation barriers requires exact values of thermodynamic data for each oxide that are unavailable. Nevertheless, the heterogeneous epitaxial nucleation barrier is usually smaller than the homogeneous one and, thus, epitaxial growth should always be promoted at the right conditions.[2d, 29a]

The physical properties of the films investigated are likely influenced by their degree of epitaxy and the local microstructure. **Figure S8a** shows the measurement of electrical resistivity for LNO films annealed at 700 ºC by RTA (20 ºC s^{-1} for 15 min) and CTA (0.5 ºC s^{-1} for 1 h). The metallic response of LNO films is remarkably good with values comparable to those reported in the literature.[35] The higher electrical resistivity values observed for the sample annealed by RTA is caused by the large amount of microstructural defects accumulated at low angle GB as compared to films grown by CTA, i.e. grain coalescence after 2D grain nucleation has not been fully completed and, hence, some intergranular pores remain.[6a] The longer dwell times used in CTA allow for additional healing of GB defects (**Figure S9a** and S9b), and thus, lower resistivity values [36]. We conducted PFM measurements for BST films grown at 900 ºC by RTA (20 ºC s^{-1} for 45 min) and CTA (0.5 ºC s^{-1} for 4 h). Figure S8b presents the dependence of the effective piezoelectric constant d_{33} as a function of the electric field which have been extracted from amplitude and phase loops

reported in the Supporting Information (**Figure S10**). The inset shows the results of writing experiments obtained by polarizing inverse ferroelectric domains at ±7 V. The loops have good saturation shapes with coercive fields of 6.2-7.5×10^7 V m^{-1}. The values of the piezoelectric constant for an AC voltage of 2.5 V and a resonance frequency of 130 kHz are approximately 8.5 (900 ºC, 20 ºC s^{-1}, 45 min) and 27 pm V^{-1} (900 ºC, 0.5 ºC s^{-1}, 4 h). These values are lower than the d_{33} constant for bulk $BaTiO_3$ ($d_{33}^{BTO\,bulk}$~190 pm V^{-1})[37], equivalent to those reported for highly (001)-oriented $BaTiO_3$ layers produced by conventional thermal CSD on (001)LNO/Pt/TiO_2/SiO_2/Si substrates,[38] and larger than those reported for thicker epitaxial $Ba_{0.6}Sr_{0.4}TiO_3$ films grown on LAO substrates.[39] It is known that the formation of piezoelectric domains is hindered at GBs which decrease the spontaneous polarization.[36] Films with small grains, i.e. those produced by RTA, have a large amount of GBs as compared to films processed by CTA with longer annealing times (Figures S9c and S9d) which explains the enhanced piezoelectric response of films produced by CTA.

2.3. Route towards thick epitaxial films

The long annealing times required to achieve full epitaxy in the investigated thick films (~60 nm) demand clearly to adopt a different strategy. When multideposition is performed with intermediate pyrolysis treatments, we have shown that the corresponding epitaxial growth rates decrease strongly when the total film thickness increases because the driving force for epitaxial growth is reduced when the precursor nanoparticles coarsen (see Figure 6b). Here, we propose a different strategy to avoid this limitation in achieving thick epitaxial films. We have performed multideposition of individually grown epitaxial layers; thus, each precursor layer will grow on top of a similar one already epitaxial, i.e. after the second layer we induce an homoepitaxial growth. We have evaluated this case for BST films in order to prevent the competition between polycrystalline and epitaxial material. **Figure 8** shows a perfectly terraced surface of a BST bilayer grown on LAO at 900 ºC, 0.5 ºC s^{-1} for 4 h in O_2. XRR

measurements in Figure 8b reveal that the film thickness is twice the value of single-layer films (~72 nm). Figures 8c and 8d illustrate that the bilayer is completely epitaxial without presence of polycrystalline phases. The surface pores observed arise from an incomplete coalescence of the Volmer – Weber nucleated grains. **Figure S11** shows equivalent experiments for CZO films grown on YSZ at 900 ºC, 20 ºC s^{-1} for 30 min in O_2. Additional data can be found elsewhere.[15] Therefore, we have demonstrated that the competition between polycrystalline and epitaxial growth development which is mastered by the rather close homogeneous and heterogeneous nucleation barriers, by a reduction of the surface and interface energies due to GB healing, and by the atomic diffusion coefficients which are found to favor epitaxy. The evaluation of these parameters can be used to define very effective strategies to grow thick epitaxial CSD-derived films by multideposition of solutions separated by complete epitaxial film development.

3. Conclusions

The analysis of the isothermal evolution of single-layer films has allowed us to quantify the time dependence of the epitaxial growth rate, estimating the coarsening rates of epitaxial and polycrystalline grains, and the microstrain evolution. We have shown that three-layer films display much reduced epitaxial grain growth rates, an issue which is correlated with an enhanced coarsening of the homogeneously nucleated grains. We have concluded that different processes control the kinetics of epitaxial grain growth, coarsening of polycrystalline grains and grain boundary defect healing. Epitaxial and polycrystalline grain coarsening are demonstrated to follow a thermally-activated self-limited growth diffusion model with different diffusion coefficients, while grain boundary diffusion and zipping processes cause a faster exponential relaxation of the local film lattice (microstrain), as compared to grain coarsening processes.

The wetting condition used to evaluate the nucleation mode of the oxide films confirms the experimentally observed 3D Volmer-Weber nucleation for CZO films on YSZ and 2D layer-by-layer nucleation for LNO films on STO. However, 3D nucleation is experimentally detected for BST films on LAO substrates which contradicts the 2D nucleation mode calculated from the wetting condition. The large contribution of strain which increases the surface energy of films is the most probable cause for this change in nucleation modes.

The coexistence of polycrystalline and epitaxial material at early stages of growth reveals close values of homogeneous and heterogeneous nucleation barriers. Epitaxial crystallization is demonstrated to occur from polycrystalline material of the final oxide phase and not from intermediate phases, and the driving force is the decrease of surface and interfacial energies of the polycrystalline stage. The crystallization of individual layers is a route to adequately reach fast fully epitaxial thick films by avoiding the excessive coarsening of polycrystalline grains which reduces the surface and interface energies.

Rapid thermal annealing furnaces have proved to be ideal tools for the study of CSD-derived oxide film grain coarsening and epitaxial crystallization, and to enhance growth rates. The fast heating ramps achieved compared with tubular furnaces have given access to very short annealing times, and allowed a precise study of nucleation modes and growth mechanisms of complex oxides. The thorough investigation of different CSD-derived oxide films, as well as the theoretical modelling employed, has provided further insight on the mechanisms involved on CSD epitaxial growth of functional oxide films, and has shown a path to develop larger epitaxial film thickness at enhanced growth rates. We have also successfully correlated film physical properties with GB healing mechanisms which indicates that longer annealing times contribute to the improvement of film functionality. These methods and studies have been proved to be of general validity for complex oxides, and so they could be easily implemented on a wide range of epitaxial systems to evaluate their growth mechanisms, but also to

optimize the industrial fabrication of functional devices for example by inkjet printing methods.

4. Experimental Section

Chemical solution deposition (CSD) is the method used to grow the functional oxide films. Solution synthesis of the oxides investigated has been described before.[31b, 40] Briefly, cerium (III) and zirconium (IV) acetylacetonate salts (Sigma-Aldrich) are added in propionic acid and stirred at 50 ºC for 30 min to obtain 0.25 M $Ce_{0.9}Zr_{0.1}O_{2-y}$ (CZO) precursor solutions. Secondly, lanthanum (III) nitrate and nickel (II) acetate precursor salts (Sigma-Aldrich) are diluted in 2-methoxyethanol and refluxed at 125 ºC for a few hours to prepare 0.2 M $LaNiO_3$ (LNO) solutions. Finally, barium (II) and strontium (II) acetate salts (Sigma-Aldrich) are mixed in propionic acid for 3 h with the addition of titanium (IV) isopropoxide to synthesize $Ba_{0.8}Sr_{0.2}TiO_3$ (BST) precursor solutions with a 0.3 M concentration. Solutions are then stabilized with acetylacetone. The CZO, LNO and BST precursor solutions are respectively spun at 6000 rpm for 2 min onto thoroughly cleaned Y_2O_3:ZrO_2 (YSZ), $LaAlO_3$ (LAO) and $SrTiO_3$ (STO) single crystal substrates (Crystec Gmbh). The substrates have a (001) orientation and are 5 x 5 mm^2 in size. The films with metalorganic precursors of CZO, LNO and BST are respectively heated at 300 ºC for 30 min, 350 ºC for 30 min, and 450 ºC for 10 min with a tubular furnace. This ensures a complete decomposition of the organic material with no detectable C residues, as determined by thermogravimetric analyses and Fourier transform infrared (FTIR) spectroscopy (see **Figure S12**).[15, 41] We estimate a detection limit for the FTIR instrument (Spectrum One, Perkin Elmer) of 0.8 wt%. Crystallization of the pyrolyzed amorphous/nanocrystalline films, which have thicknesses of 25 nm for CZO and 40-45 nm for LNO and BST,[31b] is done using an AS-Micro rapid thermal annealer (Annealsys) in static oxygen environment with heating ramps up to 20 ºC s^{-1}. Temperatures of 900 ºC for CZO and BST are selected as optimal processing conditions to study grain growth

and epitaxial crystallization due to a large atomic mobility of the species at those temperatures.[6b, 42] The annealing temperature for LNO is set to 700 ºC due to a phase instability above ~800 ºC.[43] For purpose of comparison, CTA in tubular furnaces and an oxygen flow of 0.6 l min^{-1} was also performed to ascertain that gas exchange effects do not influence the microstructural evolution. Thicker films (up to ~100 nm) are prepared through two different multilayer processes that consisted of: (1) consecutive deposition and pyrolysis steps, and a final high temperature thermal treatment at the selected conditions of the whole architecture, and (2) sequential deposition, pyrolysis and high temperature growth of each layer.

The surface morphology of films is characterized by atomic force microscopy (AFM) using an Agilent 5100 system in the intermittent contact mode. MountainsMap 7.0 software (Digital Surf) is employed to examine the resulting topographic images. The structural characterization of films is done through X-ray diffraction (XRD). The crystallographic structure is determined from one-dimensional θ-2θ measurements using a Rigaku Rotaflex RU-200BV diffractometer. This system is also used to measure the film thickness by X-ray reflectometry (XRR) at low diffraction angles. 2D-XRD analyses using a Bruker GADDS system allow the quantitative evaluation of the epitaxial fraction. Additional information about the method used to calculate the epitaxial fraction can be found elsewhere.[1d, 15, 31a] In addition, (022) pole figure measurements have been performed by integrating 360 2D XRD frames collected at steps of $\Delta\varphi$=1º for t=20 s each frame. Microstrain was evaluated following the Williamson-Hall methodology described in the Supporting Material.[15, 23] These crystallization studies are supported with additional high resolution transmission electron microscopy (HRTEM) analyses. Cross-sectional specimens are prepared by mechanical polishing and ion milling and examined with FEI Tecnai F20 and JEOL J2010F microscopes operating at 200 kV with lateral resolutions of 0.14 nm. We have also characterized the physical properties of the films. The electrical resistivity of LNO films is measured using a

physical properties measurement system (PPMS) from Quantum Design Inc., setting the electrical contacts in a four-probe configuration and following the van der Pauw method.[44] The piezoresponse of BST films has been measured by piezoresponse force microscopy (PFM) using an Agilent 5500LS system in contact mode and employing conductive diamond tips (AppNano).

Supporting Information
Supporting Information is available from the Wiley Online Library or from the author.

Acknowledgements

We acknowledge financial support from Spanish Ministry of Economy and Competitiveness through the "Severo Ochoa" Programme for Centres of Excellence in R&D (SEV-2015-0496), CONSOLIDER Excellence Network (MAT2015-68994-REDC), COACHSUPENERGY project (MAT2014-56063-C2-1-R, co-financed by the European Regional Development Fund), and the projects MAT2011-28874-C02-01, ENE2014-56109-C3-3-R and Consolider Nanoselect (CSD2007-00041), and from the Catalan Government (2014-SGR-753 and Xarmae). AQ and MdlM are also grateful for JAE-Predoc fellowship from CSIC (E-08-2012-1321248 and E-08-2013-1028356, co-financed by the European Social Fund).

Received: ((will be filled in by the editorial staff))
Revised: ((will be filled in by the editorial staff))
Published online: ((will be filled in by the editorial staff))

References

[1] a) M. Dawber, K. M. Rabe, J. F. Scott, *Rev Mod Phys* **2005**, *77*, 1083; b) W. Eerenstein, N. D. Mathur, J. F. Scott, *Nature* **2006**, *442*, 759; c) I. Vrejoiu, M. Alexe, D. Hesse, U. Gosele, *Advanced Functional Materials* **2008**, *18*, 3892; d) A. Llordes, A. Palau, J. Gazquez, M. Coll, R. Vlad, A. Pomar, J. Arbiol, R. Guzman, S. Ye, V. Rouco, F. Sandiumenge, S. Ricart, T. Puig, M. Varela, D. Chateigner, J. Vanacken, J. Gutierrez, V. Moshchalkov, G. Deutscher, C. Magen, X. Obradors, *Nat Mater* **2012**, *11*, 329; e) E. P. Murray, T. Tsai, S. A. Barnett, *Nature* **1999**, *400*, 649; f) N. Dix, R. Muralidharan, M. Varela, J. Fontcuberta, F. Sanchez, *Applied Physics Letters* **2012**, *100*, 122905; g) A. Gupta, R. Gross, E. Olsson, A. Segmüller, G. Koren, C. C. Tsuei, *Physical Review Letters* **1990**, *64*, 3191; h) E. J. Moon, B. A. Gray, A. Pimpinelli, M. Kareev, D. Meyers, J. Chakhalian, *Cryst. Growth Des.* **2013**, *13*, 2256; i) M. S. Bhuiyan, M. Paranthaman, K. Salama, *Superconductor Science and Technology* **2006**, *19*, R1; j) X. Obradors, T. Puig, *Superconductor Science and Technology* **2014**, *27*, 044003; k) C. Moreno, C. Munuera, S. Valencia, F. Kronast, X. Obradors, C. Ocal, *Nano Lett* **2010**, *10*, 3828.
[2] a) F. F. Lange, *Science* **1996**, *273*, 903; b) R. W. Schwartz, T. Schneller, R. Waser, *Cr Chim* **2004**, *7*, 433; c) X. Obradors, T. Puig, M. Gibert, A. Queralto, J. Zabaleta, N. Mestres, *Chemical Society Reviews* **2014**, *43*, 2200; d) N. Bassiri-Gharb, Y. Bastani, A. Bernal, *Chemical Society Reviews* **2014**, *43*, 2125; e) X. Obradors, T. Puig, S. Ricart, M. Coll, J. Gazquez, A. Palau, X. Granados, *Superconductor Science and Technology* **2012**, *25*, 123001.

[3] a) M. Vilardell, X. Granados, S. Ricart, I. Van Driessche, A. Palau, T. Puig, X. Obradors, *Thin Solid Films* **2013**, *548*, 489; b) R. Cobas, S. Muñoz-Pérez, S. Cadogan, M. C. Ridgway, X. Obradors, *Advanced Functional Materials* **2015**, *25*, 768; c) K.-Y. Shin, J.-Y. Hong, J. Jang, *Advanced Materials* **2011**, *23*, 2113.
[4] a) J. Zabaleta, M. Jaafar, P. Abellan, C. Monton, O. Iglesias-Freire, F. Sandiumenge, C. A. Ramos, R. D. Zysler, T. Puig, A. Asenjo, N. Mestres, X. Obradors, *J. Appl. Phys.* **2012**, *111*, 024307; b) M. Gibert, P. Abellán, A. Benedetti, T. Puig, F. Sandiumenge, A. García, X. Obradors, *Small* **2010**, *6*, 2716; c) M. Gibert, P. Abellan, L. Martinez, E. Roman, A. Crespi, F. Sandiumenge, T. Puig, X. Obradors, *CrystEngComm* **2011**, *13*, 6719; d) M. Gibert, T. Puig, X. Obradors, *Surf Sci* **2007**, *601*, 2680.
[5] a) H. Hu, C. J. Peng, S. B. Krupanidhi, *Thin Solid Films* **1993**, *223*, 327; b) M. Es-Souni, A. Piorra, *Materials Research Bulletin* **2001**, *36*, 2563; c) J. L. M. Rupp, A. Infortuna, L. J. Gauckler, *Acta Materialia* **2006**, *54*, 1721; d) A. Cavallaro, F. Sandiumenge, J. Gàzquez, T. Puig, X. Obradors, J. Arbiol, H. C. Freyhardt, *Advanced Functional Materials* **2006**, *16*, 1363; e) J. L. M. Rupp, B. Scherrer, A. S. Harvey, L. J. Gauckler, *Advanced Functional Materials* **2009**, *19*, 2790; f) V. Mihalache, I. Pasuk, *Acta Materialia* **2011**, *59*, 4875.
[6] a) X. Obradors, F. Martínez-Julián, K. Zalamova, V. R. Vlad, A. Pomar, A. Palau, A. Llordés, H. Chen, M. Coll, S. Ricart, N. Mestres, X. Granados, T. Puig, M. Rikel, *Physica C: Superconductivity* **2012**, *482*, 58; b) M. Coll, J. Gàzquez, R. Huhne, B. Holzapfel, Y. Morilla, J. García-López, A. Pomar, F. Sandiumenge, T. Puig, X. Obradors, *Journal of Materials Research* **2009**, *24*, 1446; c) X. Obradors, T. Puig, A. Pomar, F. Sandiumenge, N. Mestres, M. Coll, A. Cavallaro, N. Roma, J. Gazquez, J. C. Gonzalez, O. Castano, J. Gutierrez, A. Palau, K. Zalamova, S. Morlens, A. Hassini, M. Gibert, S. Ricart, J. M. Moreto, S. Pinol, D. Isfort, J. Bock, *Supercond Sci Tech* **2006**, *19*, S13.
[7] a) T. Dechakupt, G. Yang, C. A. Randall, S. Trolier-McKinstry, I. M. Reaney, *J Am Ceram Soc* **2008**, *91*, 1845; b) K. Daoudi, C. S. Sandu, V. S. Teodorescu, C. Ghica, B. Canut, M. G. Blanchin, J. A. Roger, M. Oueslati, B. Bessaïs, *Crystal Engineering* **2002**, *5*, 187.
[8] a) R. Pascual, M. Sayer, C. V. R. V. Kumar, L. Zou, *J. Appl. Phys.* **1991**, *70*, 2348; b) L. Jian, Z. Yi, T. Ikehara, T. Mihara, R. Maeda, "Effects of Rapid Thermal Annealing on Nucleation and Growth Behavior of Lead Zirconate Titanate Films", presented at *Applications of Ferroelectrics, 2007. ISAF 2007. Sixteenth IEEE International Symposium on*, 27-31 May 2007, 2007; c) G. González-Aguilar, I. M. Miranda Salvado, M. E. Costa, *Thin Solid Films* **2009**, *517*, 5728.
[9] a) H. Hahn, A. Sidorenko, I. Tiginyanu, *Nanoscale Phenomena: Fundamentals and Applications*, Springer, **2009**; b) G. Kostorz, *Phase Transformations in Materials*, Wiley-VCH Verlag GmbH & Co. KGaA, **2001**; c) B. M. Kulwicki, *Journal of Physics and Chemistry of Solids* **1984**, *45*, 1015; d) M. G. Blamire, J. L. MacManus-Driscoll, N. D. Mathur, Z. H. Barber, *Advanced Materials* **2009**, *21*, 3827.
[10] a) L. Tye, N. A. El-Masry, T. Chikyow, P. McLarty, S. M. Bedair, *Applied Physics Letters* **1994**, *65*, 3081; b) C. A. Copetti, H. Soltner, J. Schubert, W. Zander, O. Hollricher, C. Buchal, H. Schulz, N. Tellmann, N. Klein, *Applied Physics Letters* **1993**, *63*, 1429; c) E. Bartolomé, V. R. Vlad, A. Calleja, M. Aklalouch, R. Guzmán, J. Arbiol, X. Granados, A. Palau, X. Obradors, T. Puig, A. Usoskin, *Superconductor Science and Technology* **2013**, *26*, 125004.
[11] a) W. C. Chueh, C. Falter, M. Abbott, D. Scipio, P. Furler, S. M. Haile, A. Steinfeld, *Science* **2010**, *330*, 1797; b) N. Izu, W. Shin, N. Murayama, *Sensors and Actuators B: Chemical* **2003**, *93*, 449; c) A. Le Gal, S. Abanades, *The Journal of Physical Chemistry C* **2012**, *116*, 13516; d) N. J. Divins, I. Angurell, C. Escudero, V. Pérez-Dieste, J. Llorca, *Science* **2014**, *346*, 620; e) F. Esch, S. Fabris, L. Zhou, T. Montini, C. Africh, P. Fornasiero, G. Comelli, R. Rosei, *Science* **2005**, *309*, 752.

[12] D. Bao, X. Yao, N. Wakiya, K. Shinozaki, N. Mizutani, *Journal of Physics D: Applied Physics* **2003**, *36*, 1217.
[13] a) N. Setter, D. Damjanovic, L. Eng, G. Fox, S. Gevorgian, S. Hong, A. Kingon, H. Kohlstedt, N. Y. Park, G. B. Stephenson, I. Stolitchnov, A. K. Taganstev, D. V. Taylor, T. Yamada, S. Streiffer, *J. Appl. Phys.* **2006**, *100*, 051606; b) A. Tombak, J. P. Maria, F. Ayguavives, G. T. Stauf, A. I. Kingon, A. Mortazawi, *IEEE Microwave and Wireless Components Letters* **2002**, *12*, 3; c) J. Zhang, M. W. Cole, S. P. Alpay, *J. Appl. Phys.* **2010**, *108*, 054103.
[14] A. I. Kingon, J.-P. Maria, S. K. Streiffer, *Nature* **2000**, *406*, 1032.
[15] A. Queraltó, in *Departament de Física*, Universitat Autònoma de Barcelona, 2015, 305.
[16] a) A. Perron, O. Politano, V. Vignal, *Surface and Interface Analysis* **2008**, *40*, 518; b) J. B. Yi, X. P. Li, J. Ding, H. L. Seet, *J Alloy Compd* **2007**, *428*, 230; c) A. González-González, G. M. Alonzo-Medina, A. I. Oliva, C. Polop, J. L. Sacedón, E. Vasco, *Physical Review B* **2011**, *84*, 155450.
[17] C. V. Thompson, R. Carel, *Journal of the Mechanics and Physics of Solids* **1996**, *44*, 657.
[18] a) J. A. Floro, E. Chason, R. C. Cammarata, D. J. Srolovitz, *MRS Bulletin* **2002**, *27*, 19; b) M. Gibert, A. Garcia, T. Puig, X. Obradors, *Physical Review B* **2010**, *82*, 165415.
[19] J. E. Burke, D. Turnbull, *Progress in Metal Physics* **1952**, *3*, 220.
[20] a) X. Tang, X. Zhu, J. Dai, Y. Sun, *Acta Materialia* **2013**, *61*, 1739; b) J.-S. Lee, S.-K. Joo, *J. Appl. Phys.* **2002**, *92*, 2658.
[21] a) A.-D. Li, D. Wu, H.-Q. Ling, M. Wang, Z. Liu, N. Ming, *Journal of Crystal Growth* **2002**, *235*, 394; b) M. H. Juang, H. C. Cheng, *Thin Solid Films* **1992**, *216*, 219.
[22] a) A. M. Rosa, E. P. d. Silva, E. Amorim, M. Chaves, A. C. Catto, P. N. Lisboa-Filho, J. R. R. Bortoleto, *Journal of Physics: Conference Series* **2012**, *370*, 012020; b) J. Yu, X. Zhao, Q. Zhao, *Journal of Materials Science Letters* **2000**, *19*, 1015.
[23] G. K. Williamson, W. H. Hall, *Acta Metallurgica* **1953**, *1*, 22.
[24] S. Hayun, S. V. Ushakov, A. Navrotsky, *J Am Ceram Soc* **2011**, *94*, 3679.
[25] a) M. Foerster, M. Iliev, N. Dix, X. Martí, M. Barchuk, F. Sánchez, J. Fontcuberta, *Advanced Functional Materials* **2012**, *22*, 4344; b) G. Kästner, U. Gösele, *J. Appl. Phys.* **2000**, *88*, 4048.
[26] L. B. Freund, S. Suresh, *Thin Film Materials: Stress, Defect Formation and Surface Evolution*, Cambridge University Press, **2003**.
[27] a) J. C. Nie, H. Yamasaki, Y. Mawatari, *Physical Review B* **2004**, *70*, 195421; b) G. Ballabio, M. Bernasconi, F. Pietrucci, S. Serra, *Physical Review B* **2004**, *70*, 075417.
[28] a) L. Guan, J. Zuo, G. Jia, Q. Liu, W. Wei, J. Guo, X. Dai, B. Liu, Y. Wang, G. Fu, *Applied Surface Science* **2013**, *264*, 570; b) R. I. Eglitis, D. Vanderbilt, *Physical Review B* **2008**, *77*, 195408; c) R. I. Eglitis, G. Borstel, E. Heifets, S. Piskunov, E. Kotomin, *J Electroceram* **2006**, *16*, 289; d) J.-P. Jacobs, M. A. S. Miguel, L. J. Alvarez, *Journal of Molecular Structure: THEOCHEM* **1997**, *390*, 193.
[29] a) D. A. Porter, K. E. Easterling, *Phase Transformations in Metals and Alloys*, Springer, **1992**; b) I. Markov, in *Fundamentals of Nucleation, Crystal Growth and Epitaxy*, World Scientific, 2003; c) A. Seifert, A. Vojta, J. S. Speck, F. F. Lange, *Journal of Materials Research* **1996**, *11*, 1470.
[30] N. Moll, M. Scheffler, E. Pehlke, *Physical Review B* **1998**, *58*, 4566.
[31] a) A. Queraltó, A. Pérez del Pino, M. de la Mata, M. Tristany, X. Obradors, T. Puig, S. Trolier-McKinstry, *Ceramics International* **2016**, *42*, 4039; b) A. Queraltó, A. Pérez del Pino, M. de la Mata, J. Arbiol, M. Tristany, X. Obradors, T. Puig, *To be published*.
[32] a) C. Moreno, P. Abellan, A. Hassini, A. Ruyter, A. P. del Pino, F. Sandiumenge, M. J. Casanove, J. Santiso, T. Puig, X. Obradors, *Advanced Functional Materials* **2009**, *19*, 2139;

b) P. Abellán, C. Moreno, F. Sandiumenge, X. Obradors, in *Transmission Electron Microscopy Characterization of Nanomaterials*, (Ed: S. S. R. C. Kumar), Springer Berlin Heidelberg, Berlin, Heidelberg 2014, 537.
[33] a) V. V. Hung, J. Lee, K. Masuda-Jindo, *Journal of Physics and Chemistry of Solids* **2006**, *67*, 682; b) M. Zinkevich, F. Aldinger, *J Alloy Compd* **2004**, *375*, 147; c) D. Bäuerle, (Ed: Springer), Springer, 2011.
[34] J. Gàzquez, F. Sandiumenge, M. Coll, A. Pomar, N. Mestres, T. Puig, X. Obradors, Y. Kihn, M. J. Casanove, C. Ballesteros, *Chem Mater* **2006**, *18*, 6211.
[35] a) R. D. Sánchez, M. T. Causa, A. Caneiro, A. Butera, M. Vallet-Regí, M. J. Sayagués, J. González-Calbet, F. García-Sanz, J. Rivas, *Physical Review B* **1996**, *54*, 16574; b) K. Sreedhar, J. M. Honig, M. Darwin, M. McElfresh, P. M. Shand, J. Xu, B. C. Crooker, J. Spalek, *Physical Review B* **1992**, *46*, 6382.
[36] Q. Yin, B. Zhu, H. Zeng, *Microstructure, Property and Processing of Functional Ceramics*, Springer Berlin Heidelberg, Berlin, Heidelberg **2010**.
[37] S. V. Kalinin, D. A. Bonnell, *Physical Review B* **2002**, *65*, 125408.
[38] Y. Guo, K. Suzuki, K. Nishizawa, T. Miki, K. Kato, *Journal of Crystal Growth* **2005**, *284*, 190.
[39] H.-X. Cao, Z.-Y. Li, *Physics Letters A* **2005**, *334*, 429.
[40] a) A. Queraltó, A. Pérez del Pino, M. de la Mata, J. Arbiol, X. Obradors, T. Puig, *Cryst. Growth Des.* **2015**, *15*, 1957; b) A. Queraltó, A. Pérez del Pino, M. de la Mata, J. Arbiol, M. Tristany, A. Gómez, X. Obradors, T. Puig, *Applied Physics Letters* **2015**, *106*, 262903.
[41] P. Roura, J. Farjas, S. Ricart, M. Aklalouch, R. Guzman, J. Arbiol, T. Puig, A. Calleja, O. Peña-Rodríguez, M. Garriga, X. Obradors, *Thin Solid Films* **2012**, *520*, 1949.
[42] C.-J. Peng, S. B. Krupanidhi, *Journal of Materials Research* **1995**, *10*, 708.
[43] P. Odier, Y. Nigara, J. Coutures, M. Sayer, *Journal of Solid State Chemistry* **1985**, *56*, 32.
[44] L. J. van der Pauw, *Philips Res. Repts.* **1958**, *13*, 1.

Figures

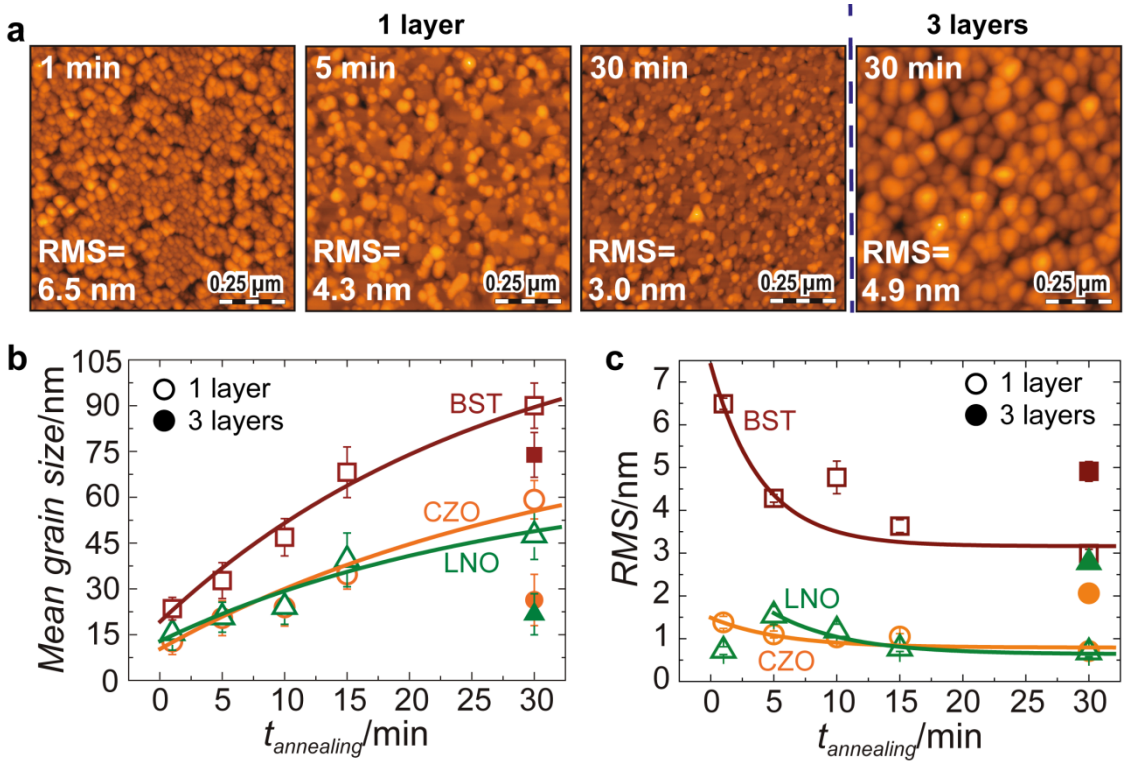

Figure 1. (a) AFM images showing the surface evolution with the annealing time ($t_{annealing}$) of BST films grown on LAO substrates by RTA. Samples were heated at a rate of 20 ºC s^{-1} up to 900 ºC and held for 1, 5 and 30 min in oxygen ambient. The right-side image after the dashed line corresponds to a film with three pyrolyzed BST precursor layers that were annealed for 30 min. Data analysis extracted from AFM: (b) mean grain size and (c) root mean square (RMS) roughness of CZO, LNO and BST films. CZO and LNO films were respectively grown on YSZ and STO substrates at 900 ºC and 700 ºC.

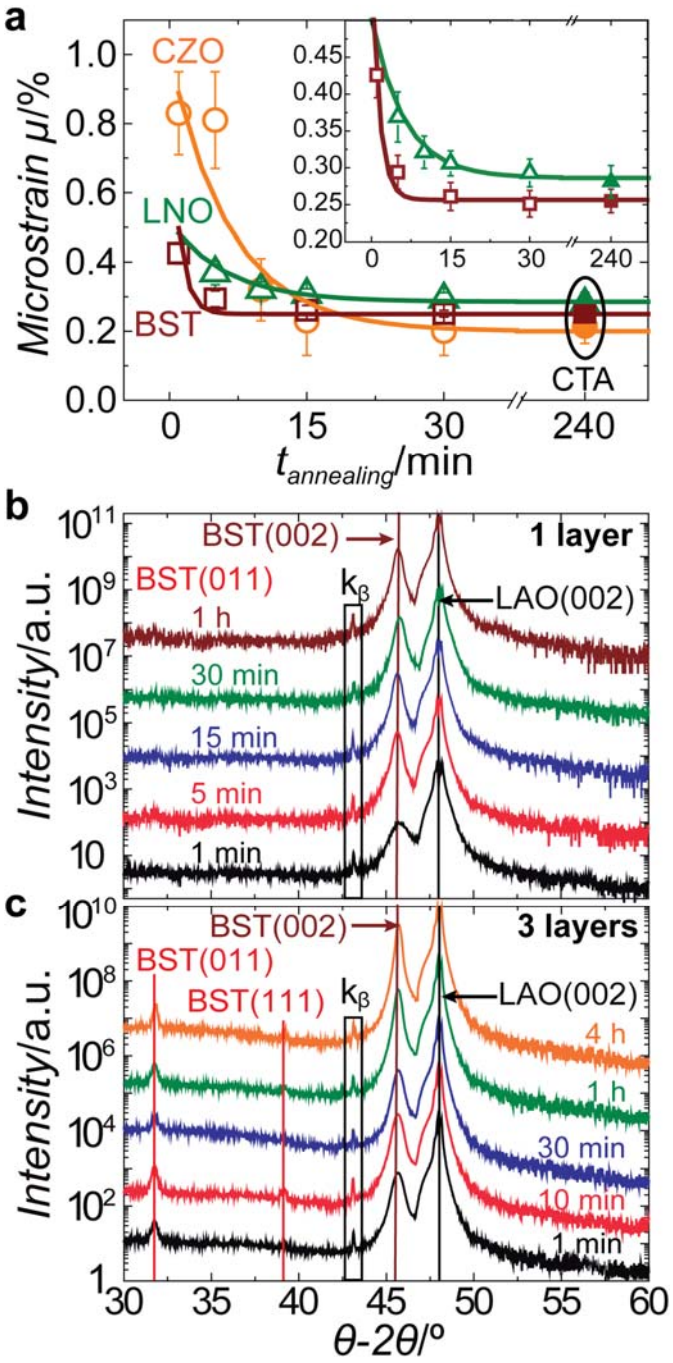

Figure 2. (a) Evolution of the microstrain relaxation (μ) of CZO, LNO and BST films during isothermal annealing time ($t_{annealing}$). Annealing temperatures: 700 ºC for LNO; 900 ºC for CZO and BST). Inset: zoomed area for better depiction of LNO and BST data. *θ-2θ* XRD measurements of BST films for (b) one and (c) three layers.

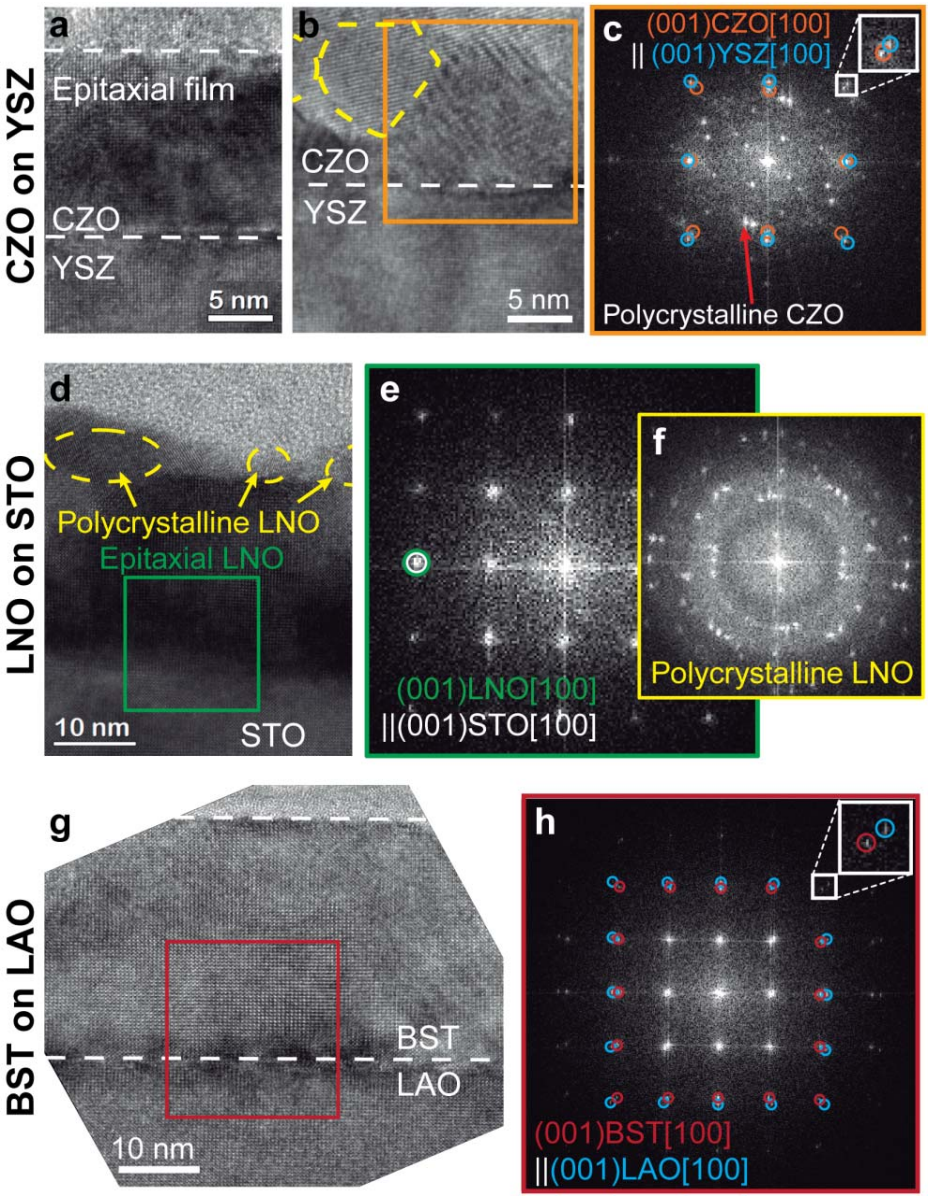

Figure 3. HRTEM characterization of single-layer CZO grown on YSZ at 900 ºC, 20 ºC s^{-1} for 10 min in O_2: (a) completely epitaxial zone, (b) partially polycrystalline area, and (c) power spectrum of the orange frame in (b). Investigation of single-layer LNO grown on STO at 700 ºC, 20 ºC s^{-1} for 10 min in O_2: (d) HRTEM image of the system, and (e) and (f) power spectra of epitaxial and polycrystalline regions. Analysis of single-layer BST grown on LAO at 900 ºC, 20 ºC s^{-1} for 5 min in O_2: (g) HRTEM image, and (h) power spectrum calculated at the colored frame in (g).

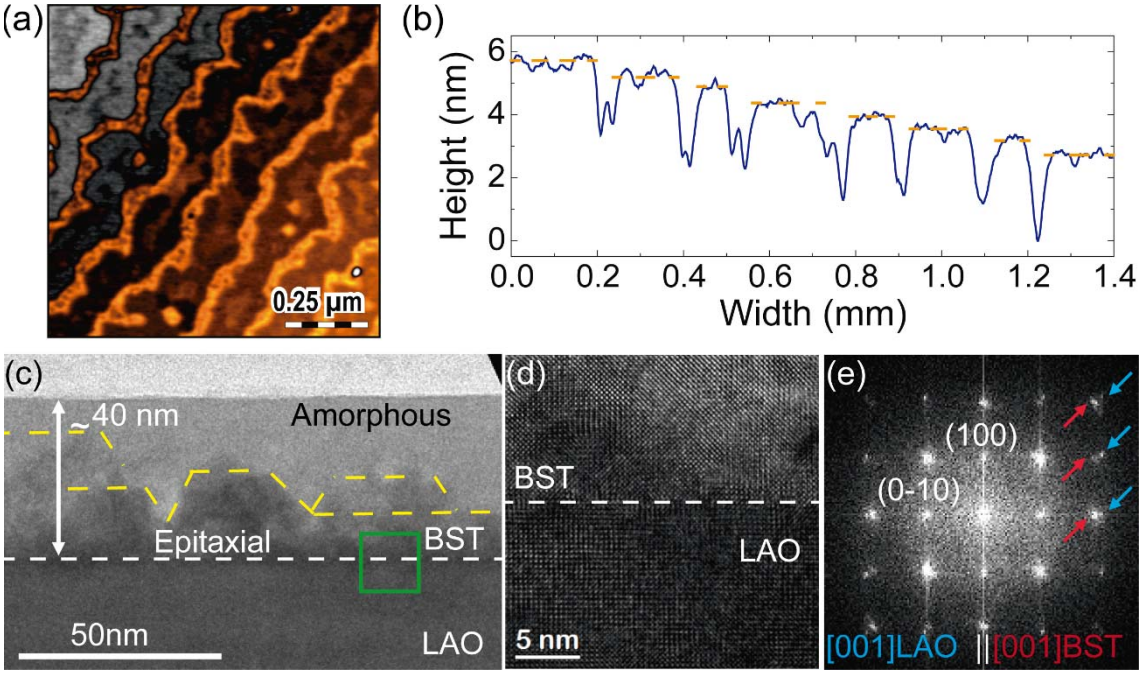

Figure 4. (a) AFM image and (b) corresponding line scan of an ultra-diluted LNO film grown on STO. The solution concentration was adjusted to 0.04 M. Growth was done at 700 ºC, 10 ºC min^{-1} for 1 h in O_2 by CTA. (c) HRTEM characterization of a BST film pyrolyzed at 450 ºC for 30 min, (d) zoom of the green area in (c), and (e) corresponding power spectrum analysis.

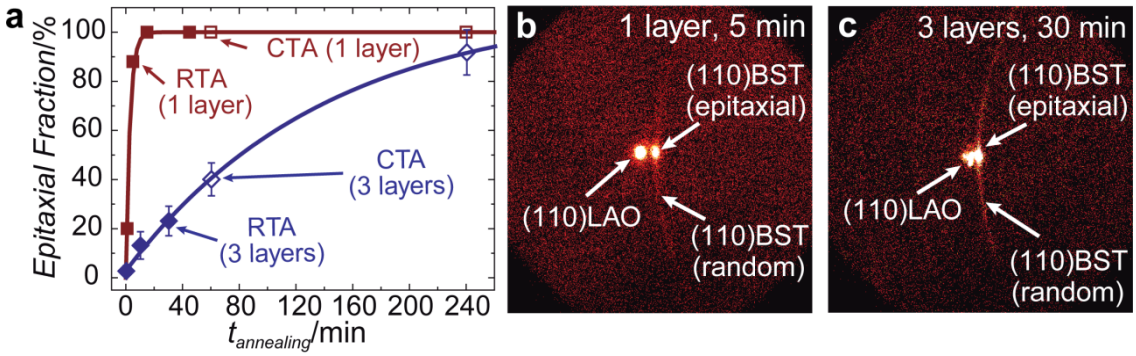

Figure 5. (a) Evolution of the epitaxial fraction with the annealing time and data fitting for one- and three-layered BST films grown on LAO substrates at 900 ºC by RTA (20 ºC s^{-1}) and CTA (0.5 ºC s^{-1}). Raw 2D-XRD data of (a) one-layered BST film annealed for 5 min, and (b) three-layered BST film annealed for 30 min.

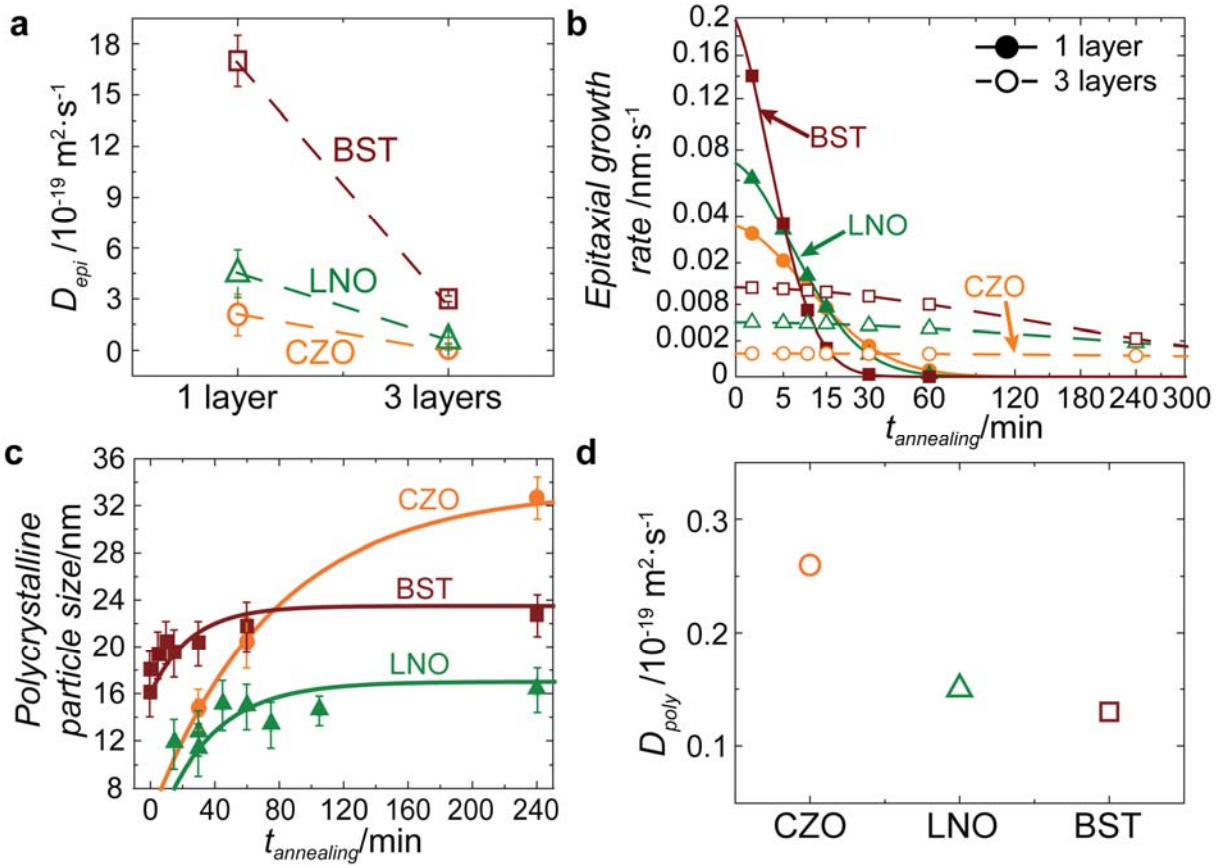

Figure 6. (a) Epitaxial diffusion coefficients (D_{epi}), and (b) dependence of the epitaxial growth rates with the annealing time ($t_{annealing}$) of one- and three-layered CZO, LNO and BST films. A scale √2 has been used in the Y-axis of (b) for better visualization. (c) Evolution of polycrystalline particle size of three-layered CZO, LNO and BST films during isothermal annealing extracted from (111)CZO, (011)LNO and (011)BST reflections. (d) Polycrystalline diffusion coefficients (D_{poly}) obtained from data in (c).

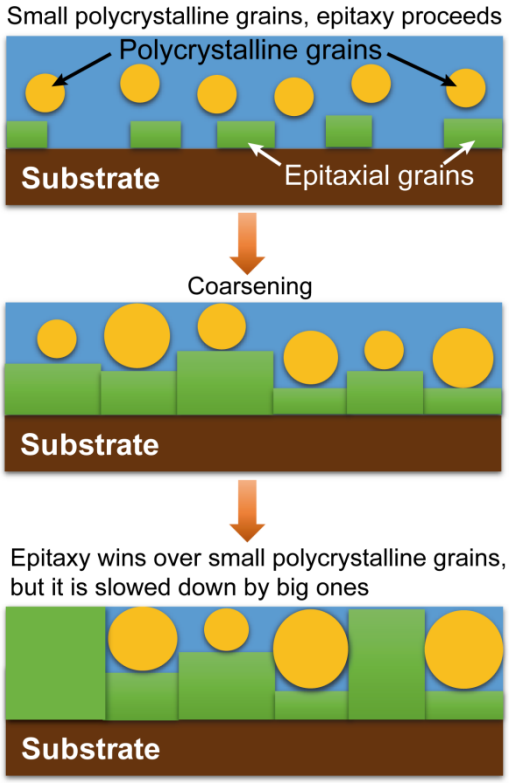

Figure 7. Schematic representation of the competition between epitaxial and polycrystalline growth in the case of Volmer-Weber heteroepitaxial nucleation mode. A similar behaviour should be expected for films with a 2D layer-by-layer nucleation.

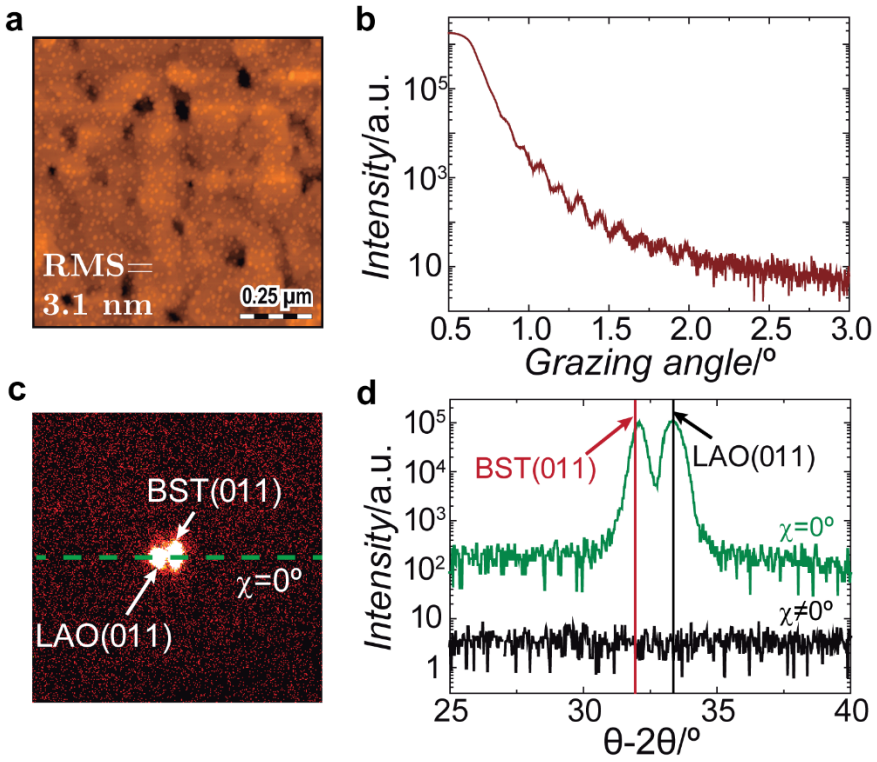

Figure 8. Growth of two independent and epitaxial BST layers on LAO: (a) AFM characterization of the surface morphology, (b) XRR measurements, (c) 2D-XRD raw data, and (d) line scan of (c) at $\chi=0^{\circ}$ and $\chi\neq0^{\circ}$.

Understanding nucleation and growth mechanisms of oxide functional materials is essential for device fabrication at industrial scale. This work investigates the relation between microstructure, epitaxial transformation and functional properties of oxide films grown by rapid thermal annealing of chemical solutions. A detailed study is conducted at different thicknesses and annealing times providing valuable information of the growth mechanisms involved.

Functional coatings

A. Queraltó*, M. de la Mata, J. Arbiol, X. Obradors, T. Puig

Disentangling Epitaxial Growth Mechanisms of Solution Derived Functional Oxide Thin Films

ToC figure 55 mm broad × 50 mm high

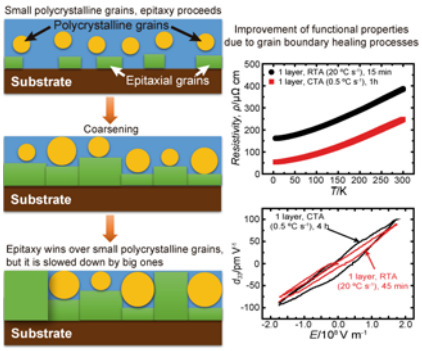

Supporting Information

Disentangling Epitaxial Growth Mechanisms of Solution Derived Functional Oxide Thin Films

Albert Queraltó, Maria de la Mata, Jordi Arbiol, Xavier Obradors, Teresa Puig*

1. Comparison between conventional and rapid thermal annealing

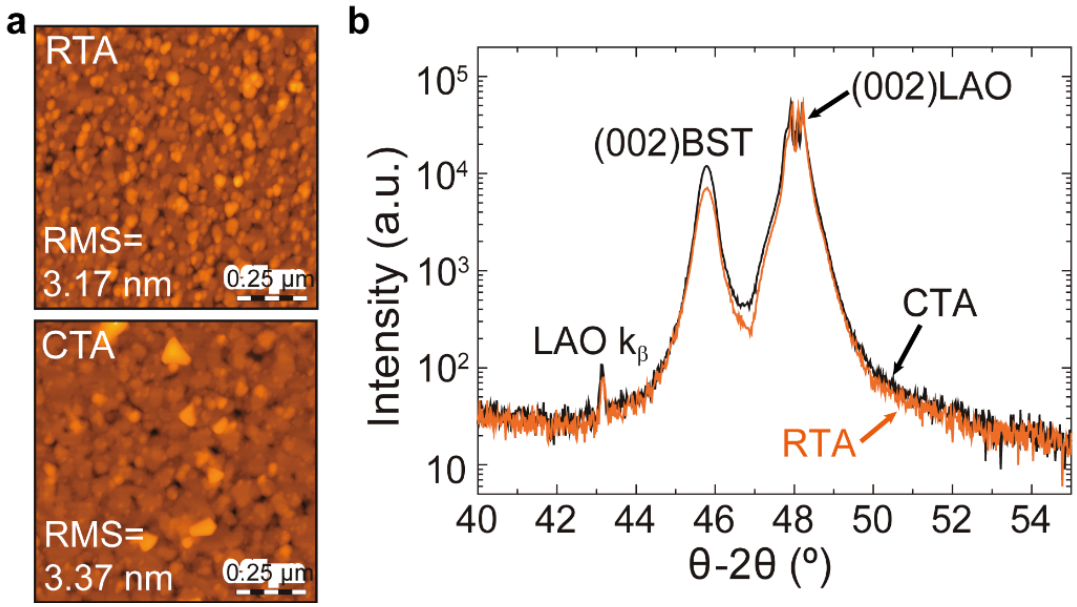

Figure S1. Comparison between conventional thermal annealing (CTA) and rapid thermal annealing (RTA). (a) AFM characterization, and (b) θ-2θ measurements of BST films heated up at 0.5 ºC s^{-1}, and held at 900 ºC for 30 min in oxygen ambient.

2. Surface morphology evolution

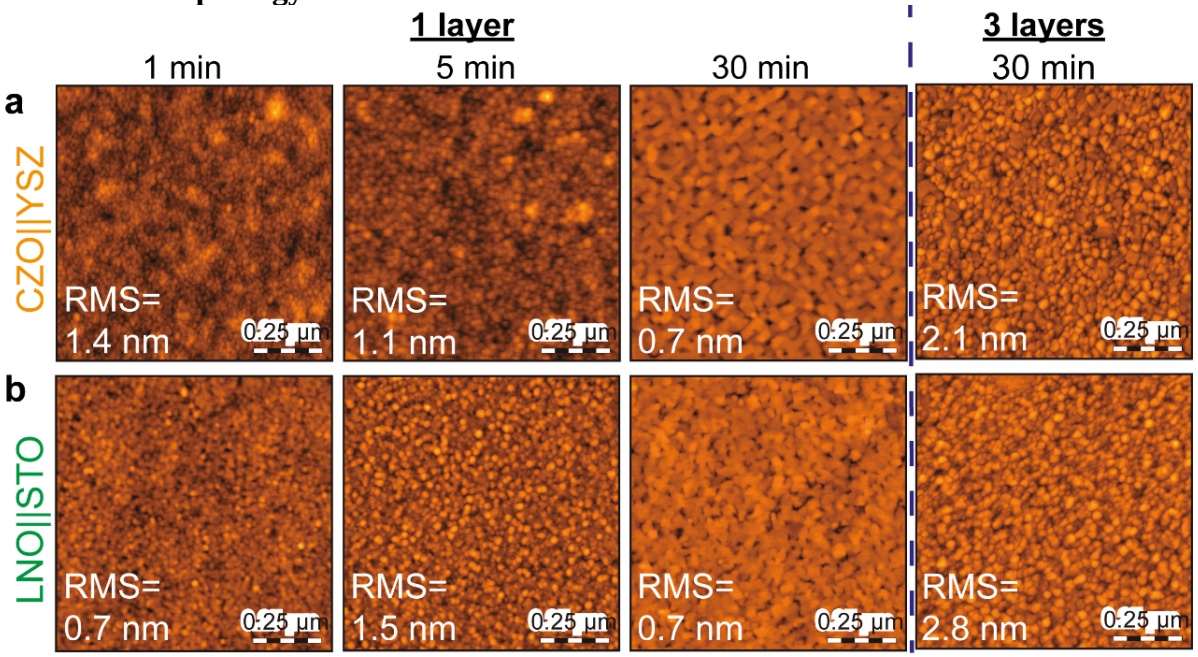

Figure S2. Characterization of the surface morphology evolution by AFM. (a) CZO and (b) LNO films grown by RTA in O_2, at 20 ºC s^{-1} up to 900 ºC and 700 ºC, respectively, and held for 1, 5 and 30 min. The images at the right side of the dashed line show films grown for 30 min after three consecutive depositions and pyrolysis of CZO and LNO precursor layers. Decomposition was at 300 ºC and 350 ºC for 30 min, respectively.

3. X-ray reflectometry of single coatings

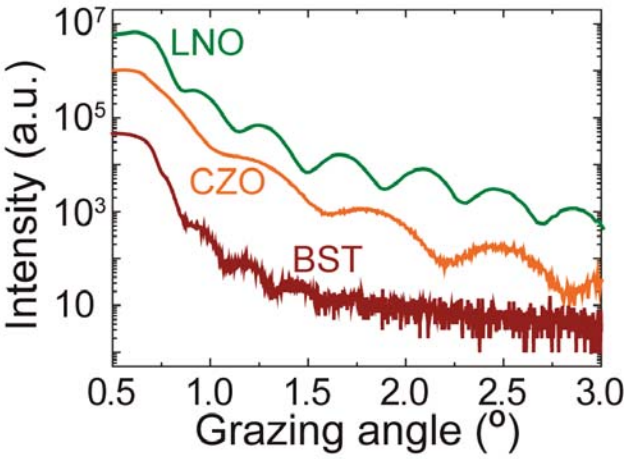

Figure S3. X-ray reflectometry (XRR) measurements of CZO, LNO and BST single coatings on YSZ, STO and LAO substrates. Films were grown by RTA at 900 ºC (CZO and BST) and 700 ºC (LNO) for 30 min in O_2. The heating was done at 20 ºC s^{-1}.

4. Microstrain relaxation of single coatings

The local crystalline structure of oxide thin films or microstructure is usually different than the ideal case, and it highly influences the functional properties. The residual stress is an important parameter controlling the film microstructure. Typically, it can be caused by processing, lattice mismatch between film and substrate, variations in the thermal expansion coefficients, and crystallographic defects such as dislocations, stacking faults, grain boundaries, etc. The measurement of lattice disorders is done by X-ray diffraction through the analysis of the shift and broadening of (hkl) peaks. The residual strain can be classified in:

- **Macrostrain (ε):** it is the long-range effect due to a uniform strain such as the change in the interplanar distance observed in early stages of heteroepitaxial film growth. It is displayed as a shift in the diffraction lines in θ-2θ measurements.
- **Microstrain (μ):** it is a short-range fluctuation in the interplanar distance caused by a non-uniform strain. It is observed as a broadening of diffraction peaks. Crystal defects (dislocations, misoriented grains, grain boundaries, mechanical deformation, etc) and grain dimensions are the main sources of microstrain.

Since the broadening associated to grain dimensions is independent of the (hkl) reflection order, the Williamson-Hall (W-H) method is the simple model to separate between both contributions. This model has been used previously in our group to calculate the microstrain of YBCO nanocomposite films [1, 2]. The method uses the different dependence of size β_s and microstrain β_m broadening on the Bragg angle θ.

$$\beta_s = \frac{K\lambda}{L\cos\theta} \quad \text{(S1)}$$

$$\beta_m = 4\mu\tan\theta \quad \text{(S2)}$$

Equation S1 corresponds to the well-known Scherrer formula where K is a constant with a value of 0.9, λ is the wavelength of the X-ray source and L is the average domain size [3]. Equation S2 where μ is the microstrain was derived by Stokes and Wilson [4]. Assuming a

Gaussian profile, the microstrain broadening is $\beta^2_{hkl} = (\beta^{exp}_{hkl})^2 - (\beta^{instr}_{hkl})^2$ and the W-H equation has the following form:

$$\beta^2_{hkl}\cos^2\theta = \left(\frac{K\lambda}{L}\right)^2 + 16\mu^2\sin^2\theta. \qquad \text{(S3)}$$

In this work, the W-H plot is used to analyze the isotropic variations of the disorder parameter along out-of-plane (00l) reflections. This is done by representing graphically the $\beta^2_{hkl}\cos^2\theta$ versus $\sin^2\theta$ for different (00l) diffraction peaks as shown in Figure S4.

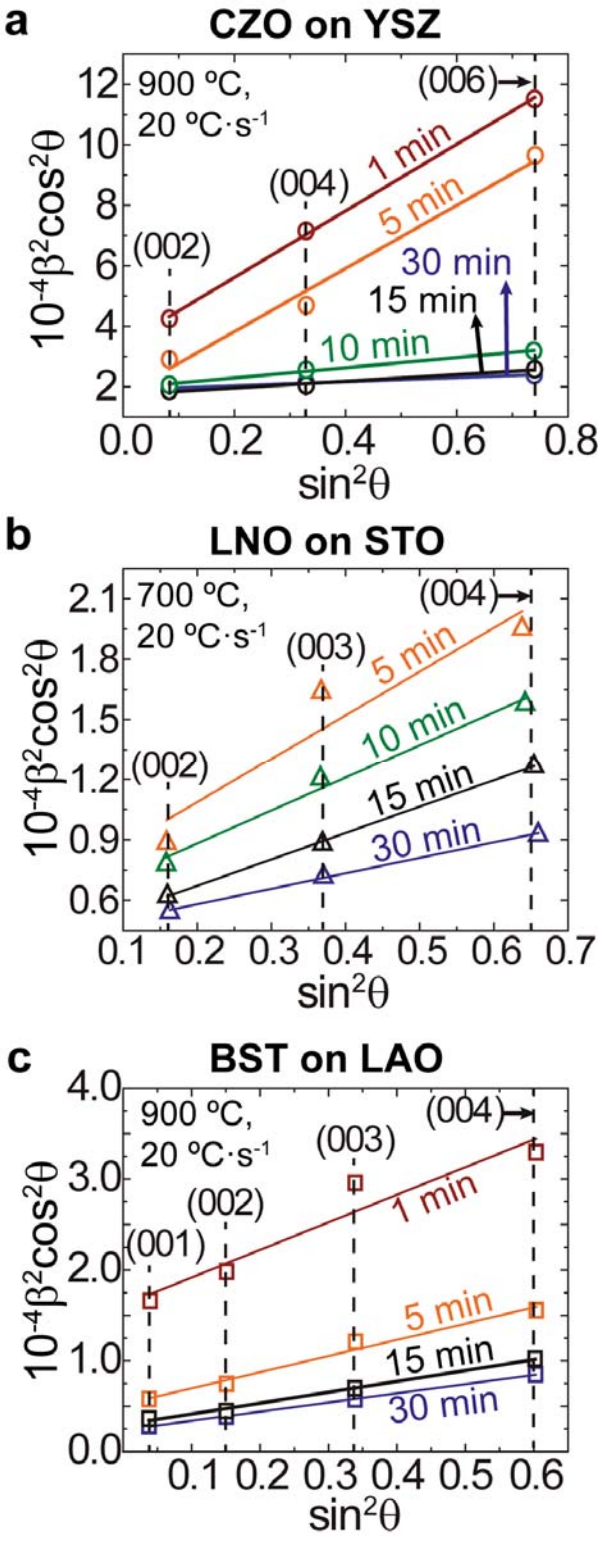

Figure S4. Microstrain analysis of (a) CZO on YSZ, (b) LNO on STO, and (c) BST on LAO. Films were grown at 900 ºC (CZO and BST) and 700 ºC (LNO) with heating ramps of 20 ºC s^{-1}.

5. One-dimensional XRD measurements

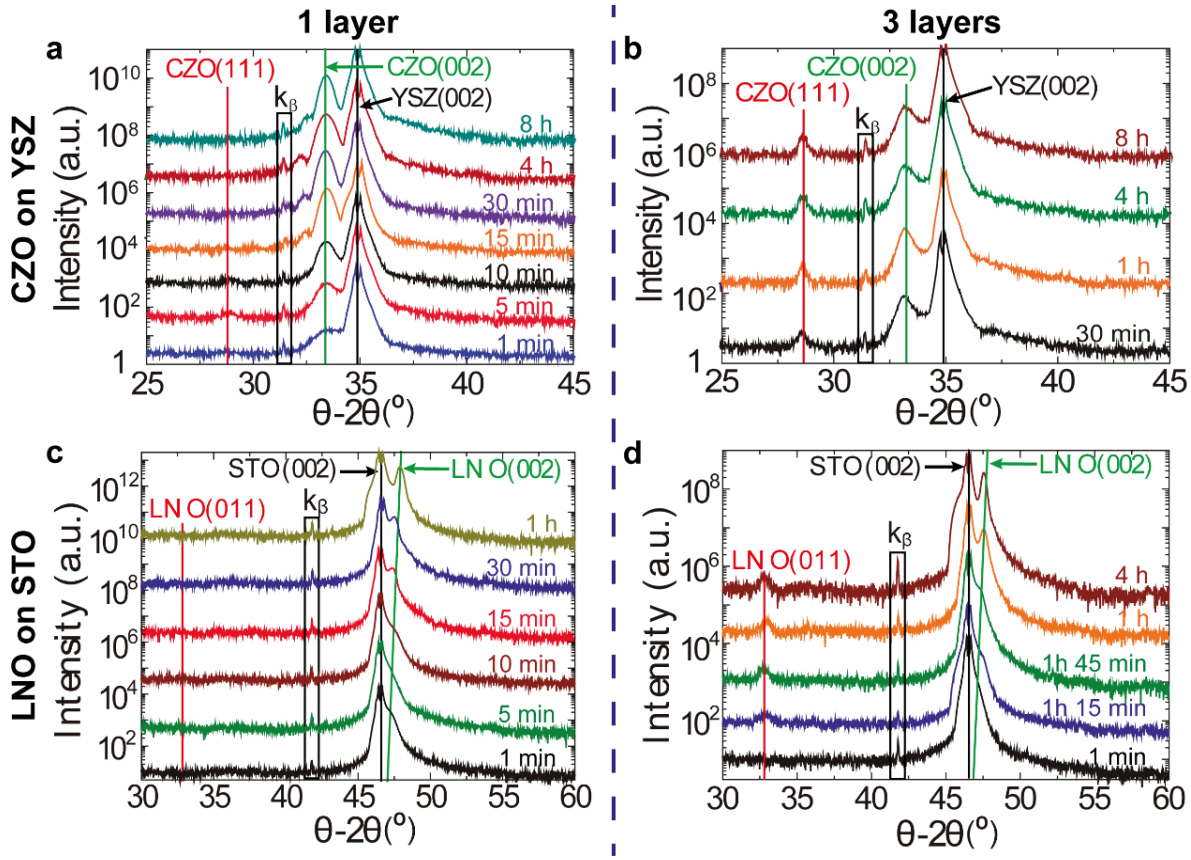

Figure S5. θ-2θ measurements at different annealing times of: (a) one and (b) three CZO layers on YSZ, and (c) one and (d) three LNO layers on STO.

6. Two-dimensional XRD measurements, epitaxial/random fractions analyses and pole figures

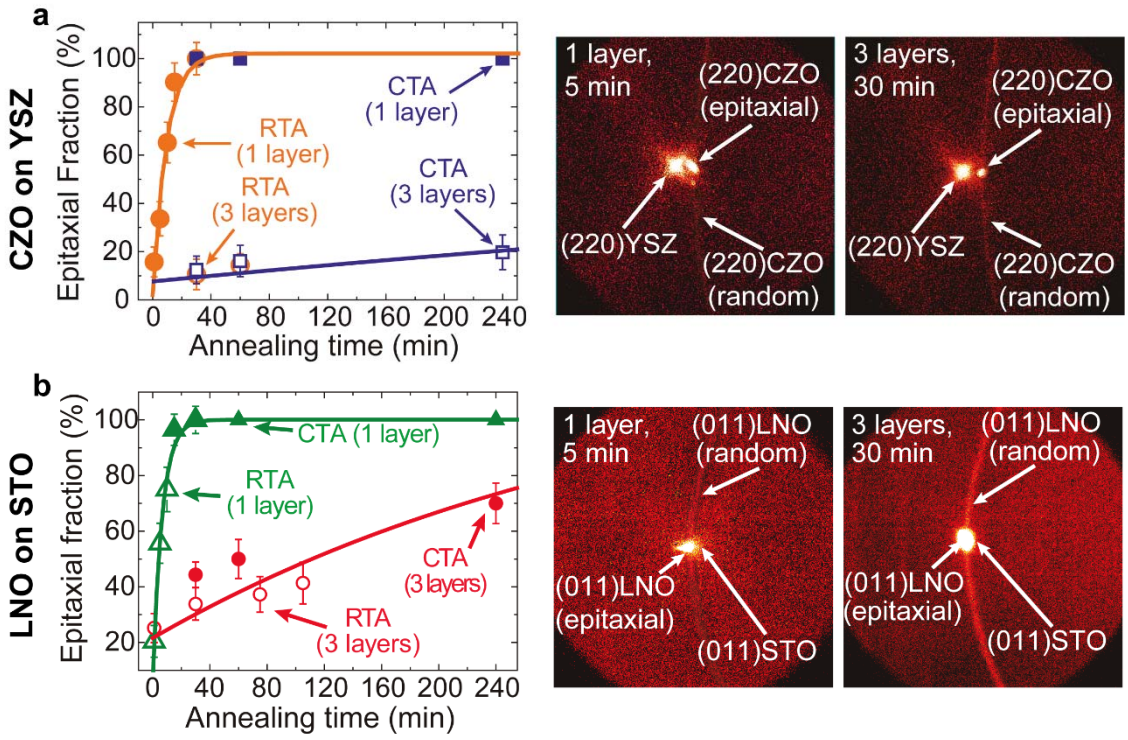

Figure S6. Epitaxial fraction of one- and three-layer films, and their corresponding 2D-XRD raw data: (a) CZO grown on YSZ at 900 ºC and (b) LNO grown on STO at 700 ºC.

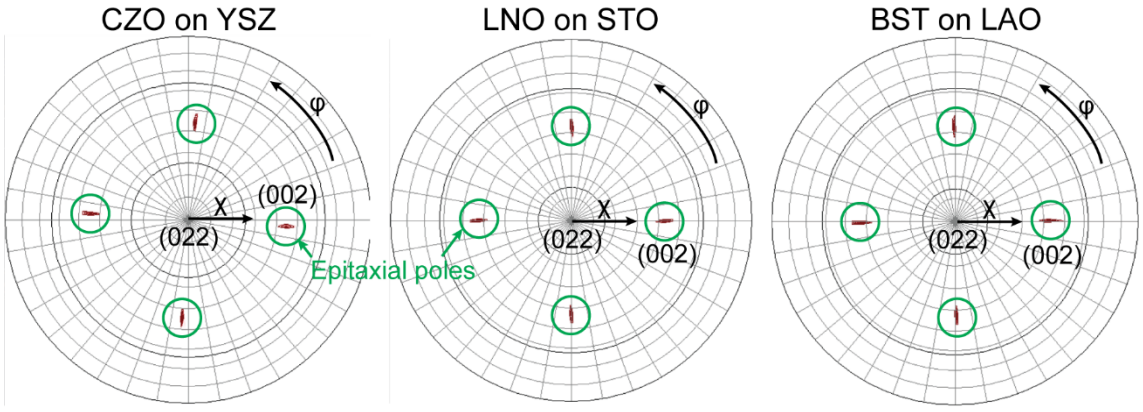

Figure S7. 2D-XRD pole figures of the (022) orientations of CZO on YSZ, LNO on STO, BST on LNO/LAO and LSMO on STO. The peaks at χ=45º correspond to the (002) epitaxial orientations. The measurements were conducted by integrating 2D frames over 360º acquired at steps of $\Delta\varphi$=1º for 20 s each frame. The films were grown by RTA at 20 ºC s^{-1}, 900 ºC for 30 min (CZO); 20 ºC s^{-1}, 700 ºC for 30 min (LNO) and 20 ºC s^{-1}, 900 ºC for 45 min (BST).

7. Physical properties of epitaxial LNO and BST films

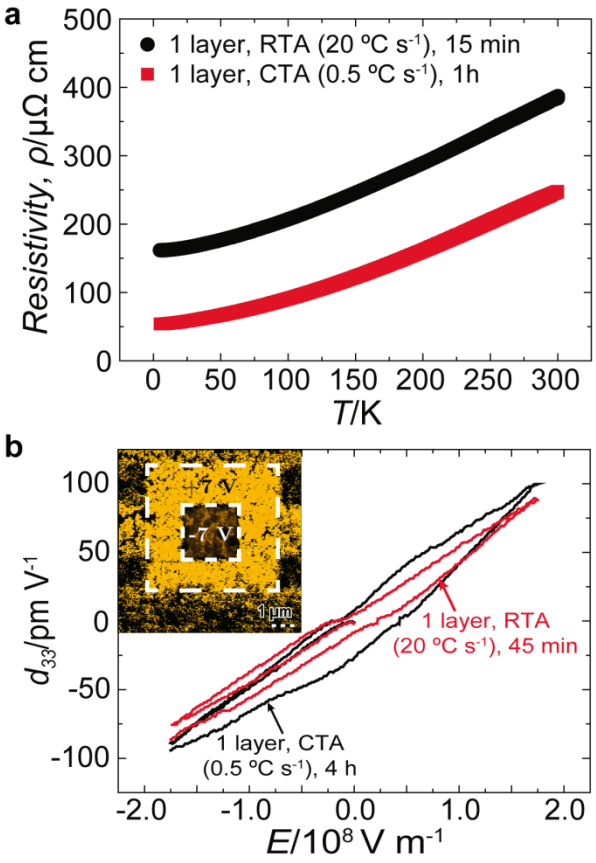

Figure S8. (a) Electrical resistivity (ρ) dependence with temperature for LNO films on STO. (b) PFM characterization of BST films on LAO showing the d_{33} constant dependence with the electric field (E). Inset: switching phase images obtained by applying ±7V. The growth conditions for each sample are indicated in their respective figure legends.

8. Surface morphology of the films used in the measurement of physical properties

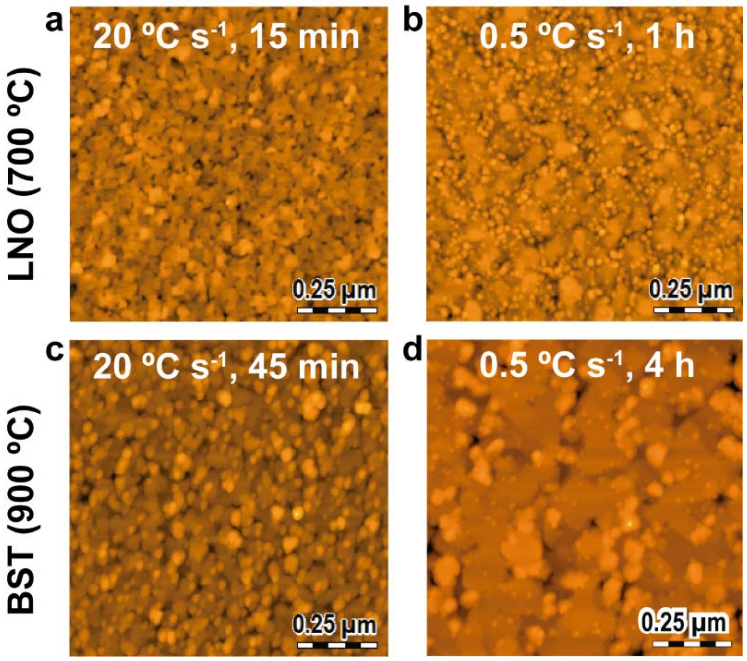

Figure S9. AFM images showing the surface morphology of the films used in the functional characterization. LNO films were annealed at (a) 700 ºC, 20 ºC s^{-1} for 15 min, and (b) 700 ºC, 0.5 ºC s^{-1} for 1 h. BST films were grown at (c) 900 ºC, 20 ºC s^{-1} for 45 min, and (b) 900 ºC, 0.5 ºC s^{-1} for 4 h.

9. Additional piezoresponse measurements

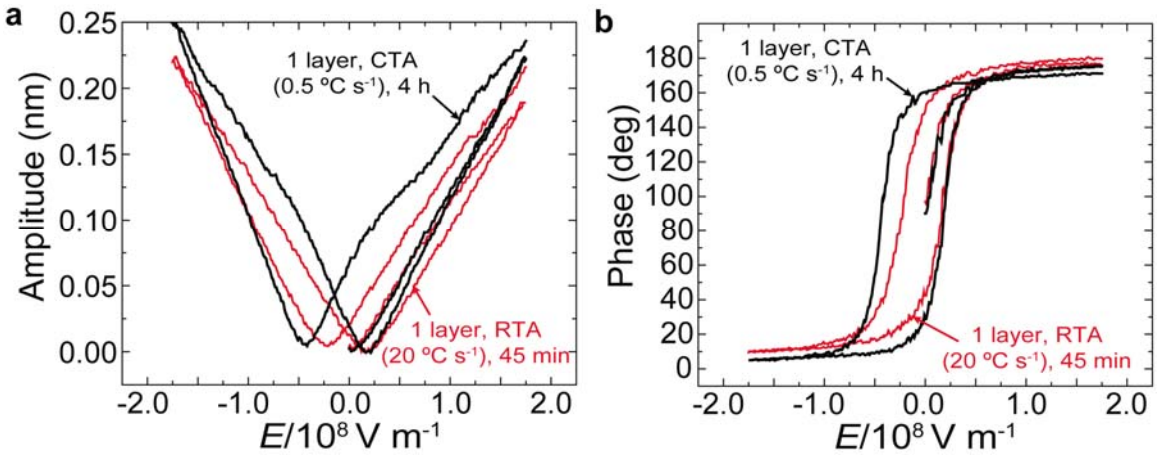

Figure S10. (a) Amplitude and (b) phase vs electric field hysteresis loops for BST films grown at 900 ºC by CTA and RTA. The specific growth conditions of each sample are indicated in the figure.

10. Growth of two independent and complete epitaxial layers

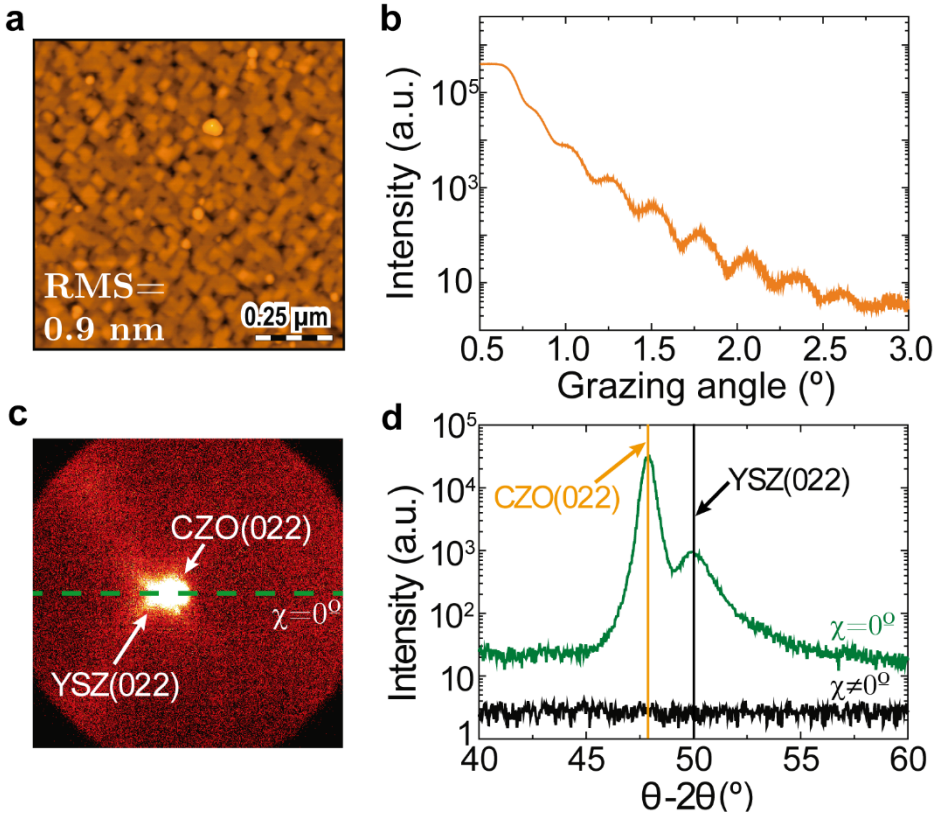

Figure S11. Growth of two independent and epitaxial CZO layers on YSZ: (a) AFM characterization of the surface morphology, (b) XRR measurements, (c) 2D-XRD raw data, and (d) line scan of (c) at χ=0º and $\chi\neq$0º.

11. FTIR spectroscopy of CZO as deposited and pyrolyzed precursor films

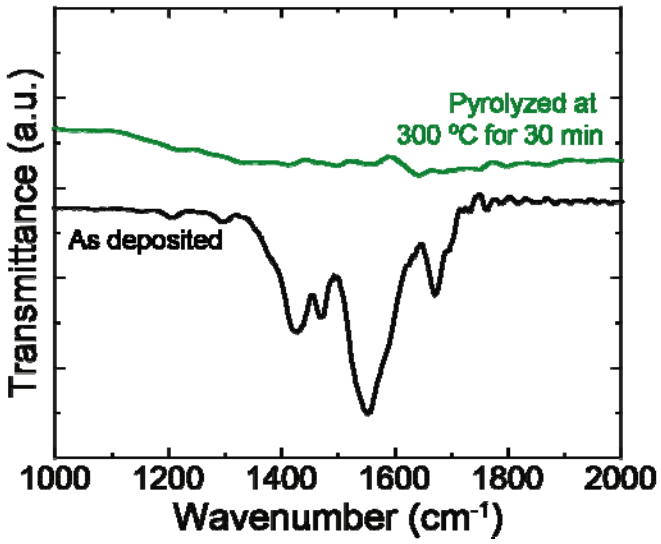

Figure S12. Fourier transform infrared spectroscopy (FTIR) measurements of an as deposited CZO precursor film and the same film pyrolyzed at 300 ºC for 30 min in O_2.

References

[1] A. Llordes, A. Palau, J. Gazquez, M. Coll, R. Vlad, A. Pomar, J. Arbiol, R. Guzman, S. Ye, V. Rouco, F. Sandiumenge, S. Ricart, T. Puig, M. Varela, D. Chateigner, J. Vanacken, J. Gutierrez, V. Moshchalkov, G. Deutscher, C. Magen, X. Obradors, Nanoscale strain-induced pair suppression as a vortex-pinning mechanism in high-temperature superconductors, Nat Mater, 11 (2012) 329-336.
[2] M. Coll, S. Ye, V. Rouco, A. Palau, R. Guzman, J. Gazquez, J. Arbiol, H. Suo, T. Puig, X. Obradors, Solution-derived $YBa_2Cu_3O_7$ nanocomposite films with a Ba_2YTaO_6 secondary phase for improved superconducting properties, Superconductor Science and Technology, 26 (2013) 015001.
[3] A.L. Patterson, The Scherrer Formula for X-Ray Particle Size Determination, Physical Review, 56 (1939) 978-982.
[4] A.R. Stokes, A.J.C. Wilson, A method of calculating the integral breadths of Debye-Scherrer lines: generalization to non-cubic crystals, Mathematical Proceedings of the Cambridge Philosophical Society, 40 (1944) 197-198.